Chinese Journal of Natural Medicines

CCA, a cassane diterpene from *Caesalpinia bonduc* ameliorates cognition impairment in Alzheimer's disease mice by regulating neuroinflammation and autophagy

Jiayu Zhou, Wei Zhang, Yiren Yang, Yue Jin, Xiaoyu Li, Yuxin Wang, Hongyuan Lu, Huiyuan Gao, Xiaowen Jiang

Citation: Jiayu Zhou, Wei Zhang, Yiren Yang, Yue Jin, Xiaoyu Li, Yuxin Wang, Hongyuan Lu, Huiyuan Gao, Xiaowen Jiang, CCA, a cassane diterpene from *Caesalpinia bonduc* ameliorates cognition impairment in Alzheimer's disease mice by regulating neuroinflammation and autophagy, Chinese Journal of Natural Medicines, 2026, 24(11), 1392−1408. doi: 10.1016/S1875−5364(26)61228−9.

View online: https://doi.org/10.1016/S1875−5364(26)61228−9

Related articles that may interest you

Bear bile powder alleviates Parkinson's disease−like behavior in mice by inhibiting astrocyte−mediated neuroinflammation
Chinese Journal of Natural Medicines. 2023, 21(9), 710−720 https://doi.org/10.1016/S1875−5364(23)60449−2

Danshen−Chuanxiongqin Injection attenuates cerebral ischemic stroke by inhibiting neuroinflammation *via* the TLR2/ TLR4−MyD88−NF− κ B Pathway in tMCAO mice
Chinese Journal of Natural Medicines. 2021, 19(10), 772−783 https://doi.org/10.1016/S1875−5364(21)60083−3

An inulin−type fructan CP−A from *Codonopsis pilosula* attenuates experimental colitis in mice by promoting autophagy−mediated inactivation of NLRP3 inflammasome
Chinese Journal of Natural Medicines. 2024, 22(3), 249−264 https://doi.org/10.1016/S1875−5364(24)60556−X

Rhodiola crenulata extract decreases fatty acid oxidation and autophagy to ameliorate pulmonary arterial hypertension by targeting inhibiton of acylcarnitine in rats
Chinese Journal of Natural Medicines. 2021, 19(2), 120−133 https://doi.org/10.1016/S1875−5364(21)60013−4

Paeoniflorin alleviates depression by inhibiting the activation of NLRP3 inflammasome *via* promoting mitochondrial autophagy
Chinese Journal of Natural Medicines. 2024, 22(6), 515−529 https://doi.org/10.1016/S1875−5364(24)60654−0

β−Elemene induces apoptosis and autophagy in colorectal cancer cells through regulating the ROS/AMPK/mTOR pathway
Chinese Journal of Natural Medicines. 2022, 20(1), 9−21 https://doi.org/10.1016/S1875−5364(21)60118−8

Wechat

Chinese Journal of Natural Medicines 24 (2026) 1392-1408

Contents lists available at ScienceDirect

Chinese Journal of Natural Medicines

journal homepage: www.cjnmcpu.com/



Original article

CCA, a cassane diterpene from *Caesalpinia bonduc* ameliorates cognition impairment in Alzheimer's disease mice by regulating neuroinflammation and autophagy

Jiayu Zhou[a,b,Δ], Wei Zhang[a,Δ], Yiren Yang[a,b,Δ], Yue Jin[a,b,Δ], Xiaoyu Li[a,b], Yuxin Wang[a,b], Hongyuan Lu[c,*], Huiyuan Gao[a,b,d,*], Xiaowen Jiang[a,b,*]

[a] *School of Traditional Chinese Materia Medica, Shenyang Pharmaceutical University, Shenyang 110016, China*
[b] *Key Laboratory of Pharmacodynamic Substances Research & Translational Medicine of Immune Diseases, Shenyang Pharmaceutical University, Shenyang 110016, China*
[c] *Department of Clinical Pharmacology, China Medical University, Shenyang 110112, China*
[d] *School of Functional Foods and Wine, Shenyang Pharmaceutical University, Shenyang 110016, China*

ARTICLE INFO

Article history:
Received 1 February 2026
Revised 26 June 2026
Accepted 19 August 2026
Available online 20 November 2026

Keywords:
Alzheimer's disease
Neuroinflammation
Autophagy
scTenifoldKnk

ABSTRACT

Alzheimer's disease (AD) is a severe neurodegenerative disorder, with persistent neuroinflammation and impaired autophagy recognized as key contributing factors. CCA is a naturally occurring cassane diterpene compound derived from the seed of *Caesalpinia bonduc*. Our research is the first to explore the role and mechanism of CCA in treating Alzheimer's disease. We assessed the levels of pro-inflammatory cytokines and autophagy in BV2 cells following lipopolysaccharide (LPS) treatment and anti-neuroinflammatory effects of CCA were evaluated in LPS-induced mice, with the underlying mechanisms explored using transcriptomic. Additionally, we examined the cognitive-enhancing effects of CCA in APP/PS1 mice and investigated *Caesalpinia bonduc* associated molecular mechanisms through proteomic analysis, immunohistochemistry (IHC) and immunofluorescence (IF) assays. Finally, the molecular target of CCA was validated using molecular dynamics simulations and cellular thermal shift assay (CETSA). CCA can down-regulate the mRNA levels of inflammatory factors in BV2 cells stimulated by LPS, and has good permeability of blood-brain barrier. Furthermore, CCA ameliorated cognitive impairment and neuronal damage in both LPS-induced and APP/PS1 mice. And demonstrated that CCA mitigates neuroinflammation by driving microglial polarization from M1 to M2, a process potentially mediated by the AMPK/NF-κB pathway, thereby reducing tau pathology. Proteomic profiling and IHC revealed that CCA upregulates FOXG1 expression in APP/PS1 mice. Furthermore, the scTenifoldKnk confirmed that AMPK has a significant impact on the regulation of autophagy and inflammation response. Our findings verified that CCA exhibits anti-neuroinflammatory activity by AMPK/NF-κB pathway and activates autophagy *via* the AMPK-mTOR-FOXG1 signaling axis, which underscores its potential as a novel therapeutic option for the treatment of AD.

1. Introduction

Alzheimer's disease (AD) is a progressive neurodegenerative disorder and is among the leading causes of dementia globally, contributing significantly to the global health burden. Clinically, AD is characterized by a gradual decline in memory and cognitive function. The primary neuropathological features of AD are the extracellular deposition of amyloid-β (Aβ) plaques and the intracellular development of neurofibrillary tangles (NFTs), the latter arising from the hyperphosphorylation of the tau protein [1]. Additionally, other molecular pathologies associated with AD include increased oxidative stress due to the accumulation of misfolded proteins, persistent neuroinflammation, and compromised autophagy [2]. In other neurodegenerative diseases such as Parkinson's disease, the treatment of neuroinflammation and the alleviation of autophagy disorders often exert neuroprotective effects [3, 4, 5]. Currently, pharmacological interventions for AD, such as donepezil, memantine, and rivastigmine, are limited to symptom management. These medications target a singular mechanism and do not possess the capability to halt or reverse the progression of AD. Moreover, they are associated with potential adverse effects, including bradycardia, gastrointestinal disturbances, and cerebral hemorrhage. Recently, Lecanemab and Donanemab have been granted marketing approval in China for the treatment of mild cognitive impairment and early-stage dementia related to AD. Clinical evidence suggests that these agents can decelerate cognitive decline in AD patients [6]. However, their efficacy is maximized when administered during the early stages of the disease. Additionally, concerns regarding their safety profiles

* Corresponding author.
E-mail addresses: 13840267257@163.com (XW. Jiang); sypugaohy@163.com (HY. Gao); hylu@cmu.edu.cn (HY. Lu)
Δ These authors contributed equally to this work.

https://doi.org/10.1016/S1875-5364(26)61228-9
Copyright © 2026, China Pharmaceutical University. Published by Elsevier B.V. All rights are reserved.

and high treatment costs present significant challenges [7]. Consequently, there is an urgent need to discover novel anti-AD therapies that are both safe and effective.

Microglial activation plays a dual and crucial role in the pathogenesis of AD. In the initial phases of AD, activated microglia exhibit neuroprotective effects by facilitating the phagocytosis and clearance of pathological proteins, including amyloid-β (Aβ) and tau [8, 9]. However, prolonged activation of microglia leads to the continuous release of pro-inflammatory factors and reduces their ability to phagocytose and degrade neurotoxic substances. This, in turn, exacerbates the accumulation of Aβ, the propagation of tau, and neuronal loss, thereby accelerating the progression of AD. Consequently, the identification of pharmacological strategies targeting neuroinflammation presents significant therapeutic potential for AD intervention [10].

Natural products offer a valuable source of bioactive compounds characterized by multi-component and multi-target mechanisms of action, which align with the complex, multifactorial pathogenesis of neurodegenerative diseases such as AD. Several compounds derived from natural products, including the clinically approved drugs galantamine and huperzine A, have demonstrated efficacy in the management of AD. Moreover, various bioactive natural compounds, including epigallocatechin gallate, quercetin, and resveratrol, are currently undergoing rigorous clinical evaluation for their therapeutic potential in AD [11].

Our previous research has demonstrated that cassane diterpenoids, which are distinctive bioactive constituents of the *Caesalpinia genus*, possess noteworthy anti-inflammatory properties [12, 13]. Subsequent investigations on *C. bonduc* and *C. minax* have yielded several cassane diterpenoids with strong anti-inflammatory effects. Notably, *Caesalpinin* M2, isolated from *C. minax*, was found to mitigate dextran sulfate sodium (DSS)-induced experimental acute colitis in mice without producing side effects akin to those of dexamethasone. These discoveries have prompted further exploration into anti-inflammatory cassane diterpenoids with novel structures from *Caesalpinia* [14]. Although previous studies by our research group have identified significant anti-inflammatory activity in *Caesalpinia bonduc* included CCA, the potential of these compounds to exert anti-neuroinflammatory effects against AD remains underexplored [15]. This study aims to investigate the effects and underlying mechanisms of the cassane diterpenoid CCA in mitigating neuroinflammation and autophagy. By elucidating the mechanisms underlying the neuroprotective effects of CCA, we hope to contribute to developing new treatment strategies for AD.

2. Material and methods

2.1. Reagents and analysis of CCA

The cassane diterpene compound CCA was derived from the seed of *Caesalpinia bonduc*. The seeds of *Caesalpinia bonduc* (Roxb.) Linn. were purchased from Bozhou Medicinal materials Market, Anhui Province, in July 2018. And identified by Prof. Jiu-Zhi Yuan (Department of Traditional Chinese Medicine, Shenyang Pharmaceutical University). The voucher specimen was deposited in the School of Traditional Chinese Materia Medica, Shenyang Pharmaceutical University (No. SY-2016-01A). The purity of CCA was over 99% at 254 nm, as detailed in **Table. S1.**

2.2. Cell culture

BV2 microglial cells were purchased from Cyagen Biosciences Inc. (Procell, China), and subsequently cultured in Minimum Essential Medium (MEM) supplemented with 10% fetal bovine serum (FBS) and 1% penicillin-streptomycin solution under standard conditions of 37 °C and 5 % CO_2.

2.3. MTT assay

BV2 cells were treated with CCA at concentrations ranging from 10 to 40 μmol·L^{-1} and incubated for 12 h. Following this incubation period, 0.5 mg·mL^{-1} MTT solution was added, and the samples were further incubated at 37 °C for 4 h. After incubation, 150 μL of DMSO was added to each well, and the plates were shaken for 10 min to ensure complete solubilization. The absorbance was then measured using a microplate reader (Varioskan Flash, FIN) at a wavelength of 490 nm.

2.4. Measurement of Nitric Oxide

BV2 cells were pretreated with 10–40 μmol·L^{-1} CCA for 6 h, followed by co-cultured with 1 μg·mL^{-1} lipopolysaccharide (LPS) for 24 h. Subsequently, 100 μL of supernatant was collected from each well to determine the concentration of nitric oxide (NO). The NO detection procedure was performed in accordance with the manufacturer's instructions provided with the Griess kit (Biyuntian, China). Briefly, following a 12-minute incubation period after mixing the cell supernatant with equal volumes of Griess Reagent A and Griess Reagent B, absorbance was measured at a wavelength of 540 nm.

2.5. PAMPA-BBB assay

Parallel artificial membrane permeation assay-BBB (PAMPA-BBB was performed to assess the brain permeability of active compounds. Four commercial drugs were used to validate the protocol and purchased from Solarbio Life Sciences. Subsequently, they were diluted 200-fold with a solution of PBS/EtOH to give a final concentration of 100 mg·mL^{-1}. The filter membrane of the donor microplate was coated with 4 mL of PBL in dodecane (20 mg·mL^{-1}). Then, 200 mL of diluted compound solution was added into the donor wells and 300 mL of PBS/EtOH. The donor filter plate was carefully placed on the top of the acceptor plate to form a "sandwich" assembly to make the membrane contact with buffer solution and put undisturbed at 25 C. After incubation for 24 h, the donor plate was carefully removed; the concentrations of test compounds in the donor and acceptor wells were measured with a UV plate spectroscopy reader [16].

2.6. ELISA assays

BV2 cells were seeded in 96-well plates at a density of 8 × 10^3 per well and incubated for 6 h under various concentrations of CCA, followed by treatment with LPS (1 μg·mL^{-1}) for 12 h. Subsequently, the supernatant was collected, and the concentrations of tumor necrosis factor-alpha (TNF-α) and interleukin-1 beta (IL-1β) in the cell supernatant were determined according to the manufacturer's instructions using ELISA kits (Elabscience, China).

2.7. Quantitative real-time PCR analysis

The hippocampus tissues or cells were lysed using the Trizol (Takara, Japan) according to the manufacturer's protocol. Total RNA was homogenized and extracted using a cryogenic grinder (Servicebio, China), followed by purification. Complementary DNA (cDNA) synthesis was carried out from total RNA using the PrimeScript RT kit (Takara, Japan). Quantitative real-time PCR analysis was conducted with TB Green Premix Ex Taq II (Takara, Japan) on a CFX96 Real-Time PCR Detection (Bio-Rad, Singapore). Tthermal cycling conditions were as follows: 95 °C for 3 min, followed by 40 cycles of 95 °C for 5 s and 60 °C for 20 s, 95 °C for 15 s, 60 °C for 60 s, 95 °C for 15 s, and 60 °C for 15 s. All primer sequences used in this study were listed in **Table. S2.**

2.8. Western blot

The brain tissues or BV2 cells were lysed with cold RIPA lysis buffer and supplemented with PMSF (Servicebio, China) at 4 ℃. The lysis buffer was collected and centrifuged at 14 000 × *g* for 10 min at 4 °C to remove cellular debris. The supernatant was collected and transferred to a 1.5 mL tube, and the total protein concentration was determined using the BCA protein assay kit (Meilun, China). SDS-polyacrylamide gel electrophoresis was carried out using appropriate gel concentrations based on the molecular weight of the target proteins. Following electrophoretic separation, the protein was transferred onto a PVDF membrane (Millipore, USA). The membrane was incubated with the corresponding primary antibody (1∶1500 dilution) overnight at 4 ℃, followed by incubation with an HRP-conjugated secondary antibody for 120 min at room temperature. Protein detection was performed using Western blotting techniques with imaging equipment from GE Healthcare (Sweden), and the obtained blot signals were quantified and analyzed using ImageJ software. The details of the primary antibodies utilized in Western blot were provided in **Table. S3**.

2.9. Cellular thermal shift assay, CETSA, (CETSA)

BV2 cells were resuspended in RIPA lysis buffer supplemented with PMSF and lysed through three freeze-thaw cycles using liquid nitrogen. The resulting cell lysates were centrifuged at 12 000 × *g* at 4 °C for 15 min. Following supernatant collection, the lysates were divided equally into two aliquots and incubated with CCA (40 μmol·L^{-1}) or an equivalent volume of DMSO at 37 °C for 1 h, respectively. Each sample was then evenly subdivided into six portions and subjected to heat treatment at 37, 42, 47, 52, 57 and 62 °C for 3 min. Afterward, loading buffer was added, followed by boiling at 100 °C for 10 min. Then, the Western blot experiment was conducted.

2.10. Animals and treatment

The familial Alzheimer's disease (APP/PS1) transgenic mice, which overexpress amyloid precursor protein (APP SWE) and presenilin 1 (PS1-DE9), along with C57BL/6 wild-type control mice, were obtained from Liaoning Changsheng Biotechnology Co., LTD. All the mice were housed under controlled environmental conditions at a room temperature of 22 ± 2 °C with a 12 h light/dark cycle. Body weights were recorded weekly and the drug was administered by gavage according to individual weight.

Ethics approval and consent to participate All procedures performed in studies involving animals were in accordance with the ethical standards of the Committee on the Ethics of Animal Experiments of the Shenyang Pharmaceutical University (No. SYPU-IACUC-S2025-0926-111)

After one week of adaptation to the feeding environment, thirty C57BL/6 mice were randomly divided into five groups: the control group, the LPS group, 10 mg·kg^{-1} CCA group, 20 mg·kg^{-1} CCA group, and the Galantamine (4 mg·kg^{-1}, positive control) group, n = 6 in each group. CCA was dissolved in 5% DMSO and formulated with 0.5% CMC-Na, which was administered orally *via* gavage for 7 days. The configuration of galantamine is the same as that of CCA, while the control group administered an equivalent volume of normal saline (wild type). On day seven post-treatment, except for the control group, all mice were intravenously injected with LPS (20 mg·kg^{-1}, 100 μL) *via* the tail vein. Following the Morris water maze experimental, all the animals were anesthetized *via* intraperitoneal administration of sodium pentobarbital, and tissue samples were collected immediately following euthanasia.

In the LPS model of C57BL/6 mice, the experimental findings indicated that, when the administration dose of CCA was 20 mg·kg^{-1}, its protective effect against neuroinflammation was more pronounced than that at a dose of 10 mg·kg^{-1}. Consequently, CCA at a dosage of 20 mg·kg^{-1} was chosen for further application in the APP/PS1 mice. Eighteen APP/PS1 mice, weighing 25–35g, were randomly allocated into three groups: APP/PS1 group, 20 mg·kg^{-1} CCA group, and 4 mg·kg^{-1} galantamine group, n = 6 in each group, with age-matched C57BL/6 mice serving as the WT group. The preparation of the CCA and galantamine is identical to that described previously. After two months of continuous administration, the Morris water maze was performed. The mice were euthanized, and their brains were extracted.

2.11. Morris water maze, (MWM)

The Morris water maze test was employed to evaluate the spatial learning and memory of the mice [17]. The experiment was conducted in a circular pool filled with a titanium dioxide solution, with a diameter of 120 cm. A hidden platform (7.5 cm in diameter) was positioned in the center of the fourth quadrant and submerged 1 cm beneath the water surface. The pool was divided into four equal quadrants, each marked with unique visual cues attached to the surrounding walls. During the testing period, the water temperature was maintained at 25 °C and the pool was enclosed with a curtain to minimize external disturbances. On the first day, the mice were placed into the pool from the first quadrant, and parameters including escape latency, number of crossings over the target platform location, and time spent in the target quadrant were recorded. On the seventh day, the platform was removed, and the mice were introduced from the fourth quadrant to assess spatial memory during the probe trial. The number of platform crossings, duration in the target quadrant, escape latency, and other relevant behavioral metrics were documented. The SuperMaze software was used for data acquisition and analysis.

2.12. Hematoxylin-eosin staining (H&E)

The mouse brain was fixed with 4% paraformaldehyde and then embedded in paraffin. Subsequently, it was sectioned into 4 μm slices using a paraffin microtome (RWD, China). The sections were dewaxed in xylene and rehydrated through a graded ethanol series. Hematoxylin staining was then carried out, followed by eosin staining after differentiation in the differentiation solution. Subsequently, the sections underwent rapid dehydration and clearing, and were mounted with neutral balsam. Histological images were captured using a Nikon microscope (Nikon, Japan) and count the number of damaged nerve cells [18].

2.13. Immunohistochemical (IHC)

Paraffin sections (4 μm in thickness) were cut, deparaffinized in xylene, and rehydrated through a graded ethanol series to distilled water. Antigen retrieval was performed using 10 mmol·L^{-1} citrate buffer (pH 6.0) to expose antigenic epitopes effectively. Endogenous peroxidase activity was blocked with 3% hydrogen peroxide solution, followed by incubation with a blocking solution (PBS containing 10% goat serum) at room temperature to reduce nonspecific antibody binding. The sections were then incubated with the primary antibody (1 ∶ 100 dilution) overnight at 4 °C. After thorough washing with PBS, the secondary antibody was applied, followed by incubation with the SABC working solution (Beyotime, China) for 30 min each at room temperature. Following three additional PBS washes, freshly prepared 3,3-diaminobenzidine (DAB) staining solution (Solarbio, China) was applied dropwise to the slides, and imaging with a

Nikon microscope (Nikon, Japan). The number and area of positive signals were quantitatively analyzed using ImageJ/Fiji software. The information of the primary antibodies used in immunohistochemistry were all presented in **Table S3.**

2.14. Immunofluorescence (IF)

A total of 1×10^4 BV2 cells per well were seeded into cell climbing plates and placed in 24-well plates. The cells were grown for 6 h with or without CCA, followed by stimulation with LPS (1 μg·mL^{-1}) for 24 h. Subsequently, the cell slides were fixed with paraformaldehyde for 15 min. After blocking, the primary antibody (1 ∶ 100 dilution) was added and incubated overnight at 4 °C. Following three washes with PBS, fluorescently labeled secondary antibodies were applied and incubated at room temperature in the dark for 1 h. After stained with DAPI, fluorescent images were captured using a fluorescence microscope (Zeiss, Germany).

For animal samples, after dewaxing and rehydration of the tissue sections, the surface antigen was repaired with high-temperature steam. Subsequently, it was incubated in the dark with 3 % hydrogen peroxide solution for 30 min to block endogenous peroxidase activity. Nonspecific antibody binding was then inhibited by incubation with a blocking solution (PBS containing 10 % goat serum) at room temperature for 1 h. After removal of the blocking solution, the primary antibodies (1 ∶ 100 dilution) were applied and incubated overnight at 4 °C. The sections were subsequently rinsed with PBS and incubated with fluorescently labeled secondary antibodies at room temperature in the dark for 1 h. Nuclear staining was performed using DAPI. An anti-fluorescence quenching mounting medium (Servicebio, China) was used to preserve fluorescence and seal the sections. Fluorescent images were captured using a confocal microscope (Nikon, Japan). Morphological features and fluorescence intensity of microglia were analyzed using ImageJ/Fiji software. The information of the primary antibody used for immunofluorescence were all presented in **Table S3.**

2.15. Nissl staining

Following dewaxing and rehydration, the tissue sections were immersed in Nissl staining solution for 3 min, subjected to mild differentiation with 0.1% glacial acetic acid, rinsed with tap water, and then baked and dried. The specimens were cleared in xylene for 10 min and subsequently mounted with neutral balsam. Histological images were captured using a Nikon microscope (Nikon, Japan).

2.16. RNA-Seq analysis

For RNA-seq analysis, partial cerebral cortical tissues were extracted from three randomly selected mice of the LPS and 20 mg·kg^{-1} CCA groups following sacrifice, with sequencing performed by Shanghai Applied Protein Technology Co., Ltd. using the Illumina Novaseq 6000/MGISEQ-T7 platform. The purified double-stranded cDNA underwent end repair, A-tail addition, and sequencing adaptor ligation, followed by fragment size selection using AMPure XP beads, and concluded with PCR enrichment to yield the final cDNA library. Subsequent to the library's construction, the insert size and effective concentration were assessed, pooled based on the target sequencing data, sequenced and aligned.

2.17. Four-dimensional-data independent acquisition (4D DIA) quantitative proteomic analysis

For 4D DIA quantitative proteomic analysis, partial cerebral cortical tissues were extracted from three randomly selected mice of the APP/PS1 and CCA groups following sacrifice. Respectively, each sample underwent protein extraction, enzymatic peptide digestion, chromatographic separation, liquid chromatography-tandem mass spectrometry (LC-MS/MS) data acquisition by Shanghai Applied Protein Technology Co., Ltd. The peptides from each sample were analyzed by TIMSTOF mass spectrometer (Bruker) connected to an Evosep One system liquid chromatography (Denmark) in the data-independent acquisition (DIA) mode. DIA data was analyzed with SpectronautTM searching the above constructed spectral library. The original DIA files were loaded into the bioinformatics database program for identification analysis, differential expression analysis, and functional analysis [19].

2.18. Bioinformatic analysis

2.18.1. Differentially expressed genes (DEGs) and differentially expressed proteins (DEPs) analysis

The obtained "Reads Per Gene" of each sample were extracted as count matrix and the differentially expressed genes were analyzed using DeSeq2 package where data were normalized by the median of the ratios. The threshold of P adj < 0.001 and the | Log fold change (Log_2 FC) | > 1.5 were used to determine the DEGs. During the analysis of DEPs, utilizing the threshold of fold change (FC) > 1.5 or FC < 0.65 (up-regulation DEPs: FC > 1.5, down-regulation DEPs: FC < 0.65), as well as P < 0.05 (*via* T-test or alternative methods) [20]. Volcano plot of the results was visualized by using the ggplot2 package at OmicStudio tools.

2.18.2. Protein-protein interaction (PPI) analysis and enrichment analysis

The DEGs were imported into the STRING database to generate a protein-protein interaction (PPI) network. Subsequently, it was imported into the Cytoscape program. The "Network Analyze" tool was chosen to assess the topological properties of the network. The Degree values were arranged in descending order, and the top 30 target genes were identified as the principal targets.

Using the Blast2Go software, the GO functional annotations were performed for all the DEPs. The GO gene sets, including molecular function (MF), biological process (BP), and cellular component (CC) categories. The pathway enrichment analysis was performed on all the DEPs using the Kyoto Encyclopedia of Genes and Genomes (KEGG) database. Visualization of Sankey using the ggsankey package at OmicStudio tools [21].

2.18.3. Single-cell sequencing data download, simulation of Gene Knockout Analysis (scTenifoldKnk) and Gene Enrichment Analysis

Single-cell RNA-sequencing datasets for Alzheimer's Disease (GSE318560) were retrieved from the GEO database (https://www.ncbi.nlm.nih.gov/geo/). This scRNA-seq dataset includes 5 healthy tissues as the control group and 6 tissues from Alzheimer's disease patients as the experimental group. Subsequently, the differential expression genes of the single-cell sequencing data were analyzed using R packages conclude "dplyr", "Seurat", "tidyverse", "patchwork", "ggplot2", "ggrepel", "remotes"and the PRKAA1 gene virtual knockout analysis was performed using the scTenifoldKnk software package. Using the raw count matrix as input, data quality control filtering, normalization, and principal component analysis (PCA) were performed sequentially. Ten gene regulatory subnetworks were constructed, from each of which 500 cells were randomly sampled. Three principal components were retained to maintain the structural characteristics of the dataset. PRKAA1 was selected as the target gene for in silico knockout, and the simulated knockout procedure was ex-

ecuted to calculate the fold change (FC), Z-score, and adjusted *P* value (*P.* adj) for each gene. Subsequently, we conducted Gene Ontology (GO) enrichment analysis and Kyoto Encyclopedia of Genes and Genomes (KEGG) enrichment analysis on the genes selected that were related to the knockout of PRKAA1. The gene-related GO and KEGG data were obtained from DAVID [22, 23]. The GO enrichment analysis and KEGG enrichment analysis of the Gene knocked-out parts was plotted by https://www.bioinformatics.com.cn (last accessed on 10 Dec 2024), an online platform for data analysis and visualization.

2.19. Statistical analysis

Statistical comparisons among multiple groups were conducted using one-way ANOVA and two-way analysis (for escape latency analysis in the MWM assay) with Tukey's post hoc test by using with GraphPad Prism 9.5 (GraphPad Software, La Jolla, California, USA). A *P*-value less than 0.05 was deemed statistically significant.

3. Results

3.1. CCA demonstrated significant anti-inflammatory effects in LPS-induced BV2 cell

To assess the anti-neuroinflammatory activity of CCA *in vitro*, we established LPS-induced BV2 neuroinflammatory cell model. Within the concentration range of 10−40 μmol·L^{-1}, CCA exhibited no detectable cytotoxicity while potently inhibiting NO production in LPS-stimulated BV2 cells in a concentration-dependent manner (Figs. 1A&1C, Fig. S1A). Morphological analysis revealed that exposure with LPS induced an amoeboid morphology in BV2 microglia, typified by a swollen cell soma and pleomorphic morphological alterations, a hallmark indicative of microglial activation and phenotypic remodeling. By contrast, CCA treatment substantially reversed these LPS-induced morphological aberrations, restoring the cells to their quiescent phenotypic status (Fig. 1B). ELISA analyses revealed that LPS treatment significantly elevated the expression levels of inflammatory cytokines such as Tumor necrosis factor alpha (TNF-α) and interleukin-1 beta (IL-1β) in BV2 cells. Conversely, CCA intervention dose-dependently attenuated the release of these proinflammatory mediators (Fig. 1D). Furthermore, qRT-PCR analysis confirmed that CCA effectively downregulated the mRNA transcription levels of pro-inflammatory cytokines, including IL-1β, Interleukin-6 (IL-6), TNF-α, and inducible Nitric Oxide Synthase (iNOS) in LPS-stimulated BV2 microglial cells (Fig. 1E). To delineate the molecular mechanisms underlying CCA-mediated anti-neuroinflammatory activity, we examined the expression and phosphorylation statuses of key proteins in the NF-κB signaling cascade *via* immunoblotting assays. The results revealed that, compared with the LPS-treated group, the phosphorylation levels of NF-κB and IκB, the protein expression levels of TNF-α and iNOS were significantly reduced in the CCA treatment group (Figs. 1F−1I). Collectively, these complementary lines of evidence at the phenotypic, protein and transcriptional levels corroborate that CCA exerts robust anti-neuroinflammatory effects in LPS-activated microglia, likely through the inhibition of proinflammatory gene expression and subsequent cytokine secretion.

3.2. CCA demonstrates favorable permeability across the blood-brain barrier in vitro

The blood-brain barrier (BBB) poses a significant obstacle in the development of therapeutics for central nervous system (CNS) diseases [24, 25]. Effective CNS drugs must be capable of penetrating the BBB to access the brain. In this study, the permeability of the BBB to CCA and selected control drugs was evaluated using the Parallel Artificial Membrane Permeability Assay (PAMPA) (Table 1). Compared to the positive control drugs, testosterone and verapamil hydrochloride, as well as the negative control drugs, enoxacin and penicillin G Na, CCA demonstrated a -log (*P*e) value of −5.43 cm·s^{-1}. This finding suggests that CCA possesses favorable BBB penetration capabilities, warranting further *in vivo* pharmacodynamic evaluation.

3.3. CCA can attenuated the cognitive impairment of LPS-induced neuroinflammation mice

To assess the anti-neuroinflammatory effects of CCA *in vivo*, a neuroinflammatory mouse model was established by intravenous injection of LPS. Flowchart of experimental procedures as show in Fig. 2A. In the MWM experiment, CCA treatment significantly shortened the escape latency of LPS-treated mice and markedly increased the number of platform crossings in the target quadrant (Figs. 2B&2C). These findings suggested that CCA effectively ameliorated spatial cognitive impairments in the LPS-induced neuroinflammatory mice model. H&E staining results revealed that, compared with the control group, LPS administration caused nuclear shrinkage in cortical neurons and a reduction in the number of granule cells in the hippocampal dentate gyrus (Figs. 2D&2E). However, in the CCA-treated group, the morphology of cortical cell nuclei was largely restored, and the number of granule cells in the dentate gyrus increased. Moreover, CCA alleviated LPS-induced liver and kidney damage in mice (Fig. S1B), suggesting its favorable safety profile. Nissl staining demonstrated a decrease in the number of Nissl bodies in the LPS group, whereas CCA treatment led to an increase of Nissl bodies in both the hippocampus and cortex (Figs. 2F&2G). These results indicated that CCA not only improved cognitive dysfunction in LPS-treated mice, but also reversed the pathology of inflammation in the cortex and hippocampus.

3.4. CCA inhibited LPS-induced neuroinflammation in mice through the NF-κB signaling pathway

To elucidate the mechanism underlying the anti-neuroinflammatory effects of CCA, we conducted RNA-Seq analysis of the cortex with CCA group mice and LPS group mice. As shown in Fig. 3A, a total of 1330 differentially expressed genes (DEGs) were identified, comprising 595 up-regulated and 735 down-regulated DEGs. PPI analysis based on the top 30 genes ranked by degree score revealed that inflammation-related genes such as IL-1β and IL-1α occupied central positions within the interaction network (Fig. 3B). Results from GO-BP functional enrichment analysis indicated significant enrichment in biological processes related to inflammatory response and cytokine receptor binding (Fig. 3C). The Sankey enrichment analysis demonstrated that the top enriched pathways including TNF signaling, NF-κB signaling, IL-17 signaling, Toll-like receptor signaling, and NOD-like receptor signaling were significantly enriched. Notably, IL1β, IL1α, and Tnfaip3 emerged as core regulatory genes across multiple pathways (Fig. 3D). Subsequently, qPCR results revealed that CCA treatment dose-dependently reduced the mRNA expression levels of pro-inflammatory cytokines, such as IL-6 and TNF-α in the hippocampus of LPS mice (Fig. 3E). Western blot analysis showed that, the LPS group exhibited significantly increased the expression levels of iNOS compared with that of control group, as well as elevated phosphorylation levels of NF-κB and IκB. However, these protein expression levels were markedly reduced in the CCA-treated LPS mice (Figs. 3F&3G). Furthermore, immunofluorescence (IF) staining revealed a significant increase in the fluorescence intensity of the microglial marker IBA1 in the dentate gyrus of hippocampal of LPS-treated mice, an effect that was notably attenuated following CCA administration (Figs. 3H&3I).

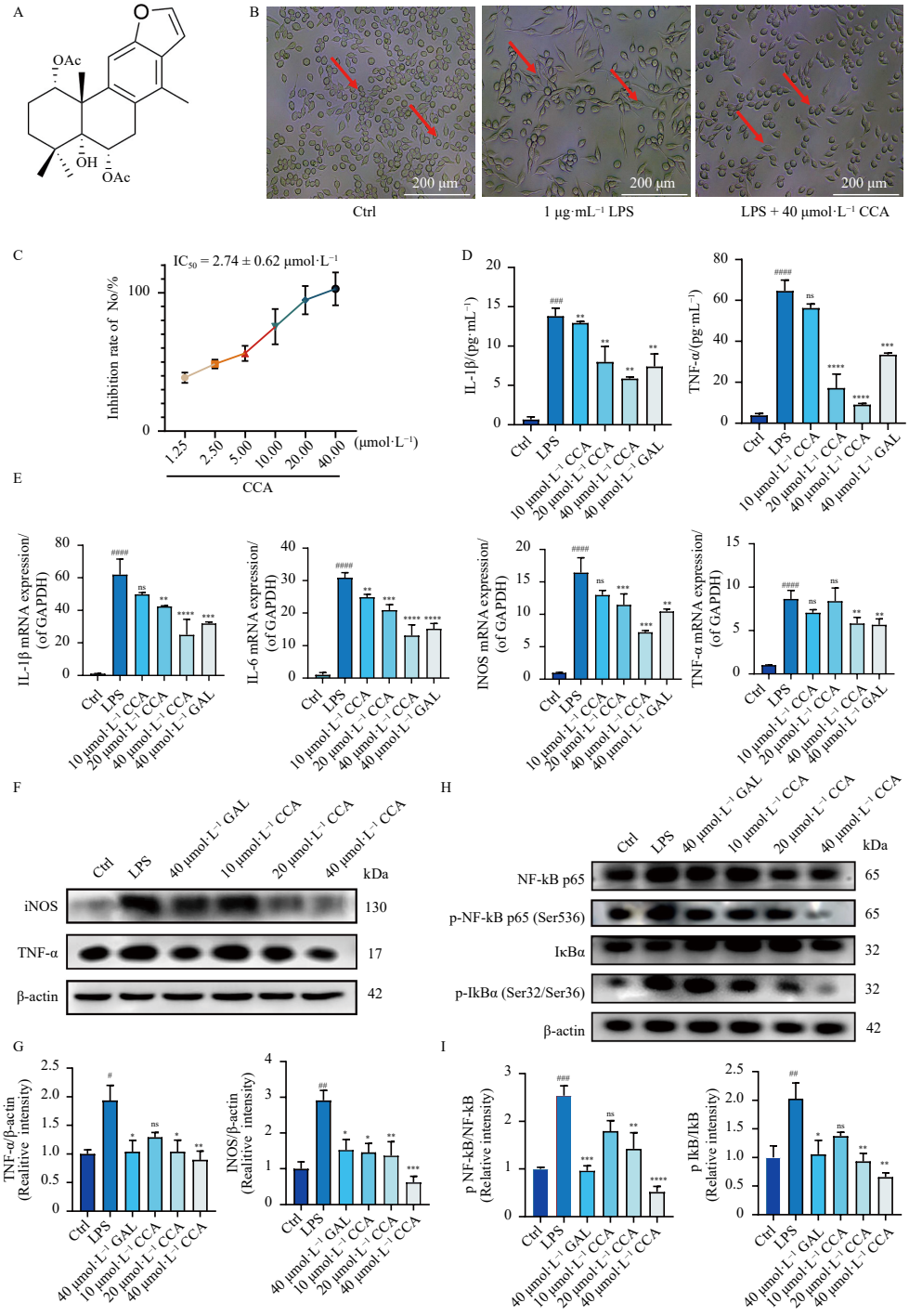


Fig. 1 CCA mitigated inflammation in BV2 cells induced by LPS. (A) Chemical structure of CCA. (B) The morphology of BV2 cells, scale bar: 200 μm. (C) The NO inhibition rate of BV2 cells after co-incubation with CCA. (D) ELISA was employed to quantify the concentrations of IL-1β and TNF-α in the supernatant of BV2 cells. (E) qRT-PCR was employed to assess the mRNA levels of the pro-inflammatory factors IL-1β, IL-6, iNOS and TNF-α. (F) Detection of iNOS, TNF-α protein expression in the BV2 cells by Western blot, with quantification shown in (G). (H) Detection of NF-κB pathway-related proteins in BV2 cells by Western blot, with quantification shown in (I). All the data are presented as the mean ± SD. One way ANOVA followed by Tukey's multiple comparisons test was conducted in the statistical analysis. $^{\#}P < 0.05$, $^{\#\#}P < 0.01$, and $^{\#\#\#}P < 0.001$ *vs* ctrl group. $^{*}P < 0.05$, $^{**}P < 0.01$, $^{***}P < 0.001$, $^{****}P < 0.0001$ *vs* LPS group, *ns* denotes no significant.

Table 1 Permeability (Pe) of commercial drugs and CCA in the PAMPA BBB assay.

Compounds	Measured wavelength (nm)	−log (*Pe*) (cm·s^{-1})	Prediction
Verapamil hydrochloride	331	−5.30 ± 0.05	CNS +
Testosterone	382	−5.05 ± 0.05	CNS +
Enoxacin	346	−6.24 ± 0.05	CNS-
Penicillin G Na	264	−6.06 ± 0.05	CNS-
CCA	390	−5.43 ± 0.05	CNS +

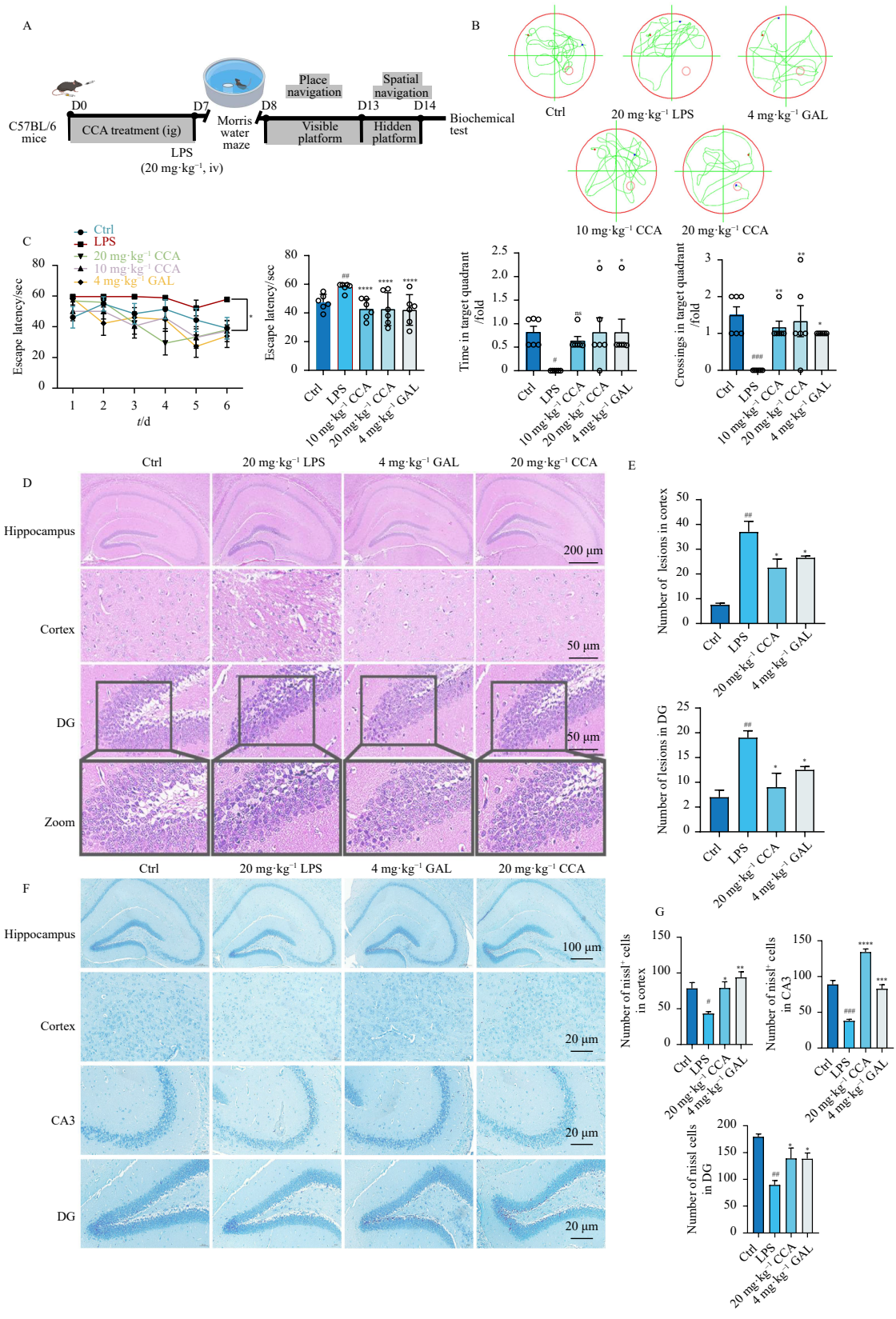


Fig. 2 CCA reversed LPS-induced cognitive dysfunction and neurological damage in LPS-stimulated C57BL/6 mice. (A) Flowchart of experimental procedures. (B) Representative photographs of the movement trajectory of mice. (C) The escape latency and the frequency of platform crossings, $n = 6$ mice. (D) H&E staining in LPS-induced mice, scale bar: 200 μm and 50 μm. (E) The quantity of lesions cells. (F) Nissl staining in LPS-induced mice, scale bar: 100 μm and 20 μm. (G) Statistics regarding the quantity of Nissl $^{+}$ bodies. All the data are presented as the mean ± SD. One way ANOVA followed by Tukey's multiple comparisons test was conducted in the statisticalanalysis. $^{\#}P < 0.05$, $^{\#\#}P < 0.01$, $^{\#\#\#}P < 0.001$, $^{\#\#\#\#}P < 0.0001$ *vs* ctrl group. $^{*}P < 0.05$, $^{**}P < 0.01$, $^{***}P < 0.001$, $^{****}P < 0.0001$ *vs* LPS group, *ns* denotes no significant.

These results suggest that CCA can inhibit LPS-induced microglial activation. Additionally, CCA treatment significantly decreased the fluorescence intensity of the M1 phenotypic marker CD86, while that of the M2 phenotypic marker CD206 was markedly increased in the dentate gyrus of CCA-treated LPS mice compared with the LPS group (Figs. 3H&3I). This indicated that CCA might

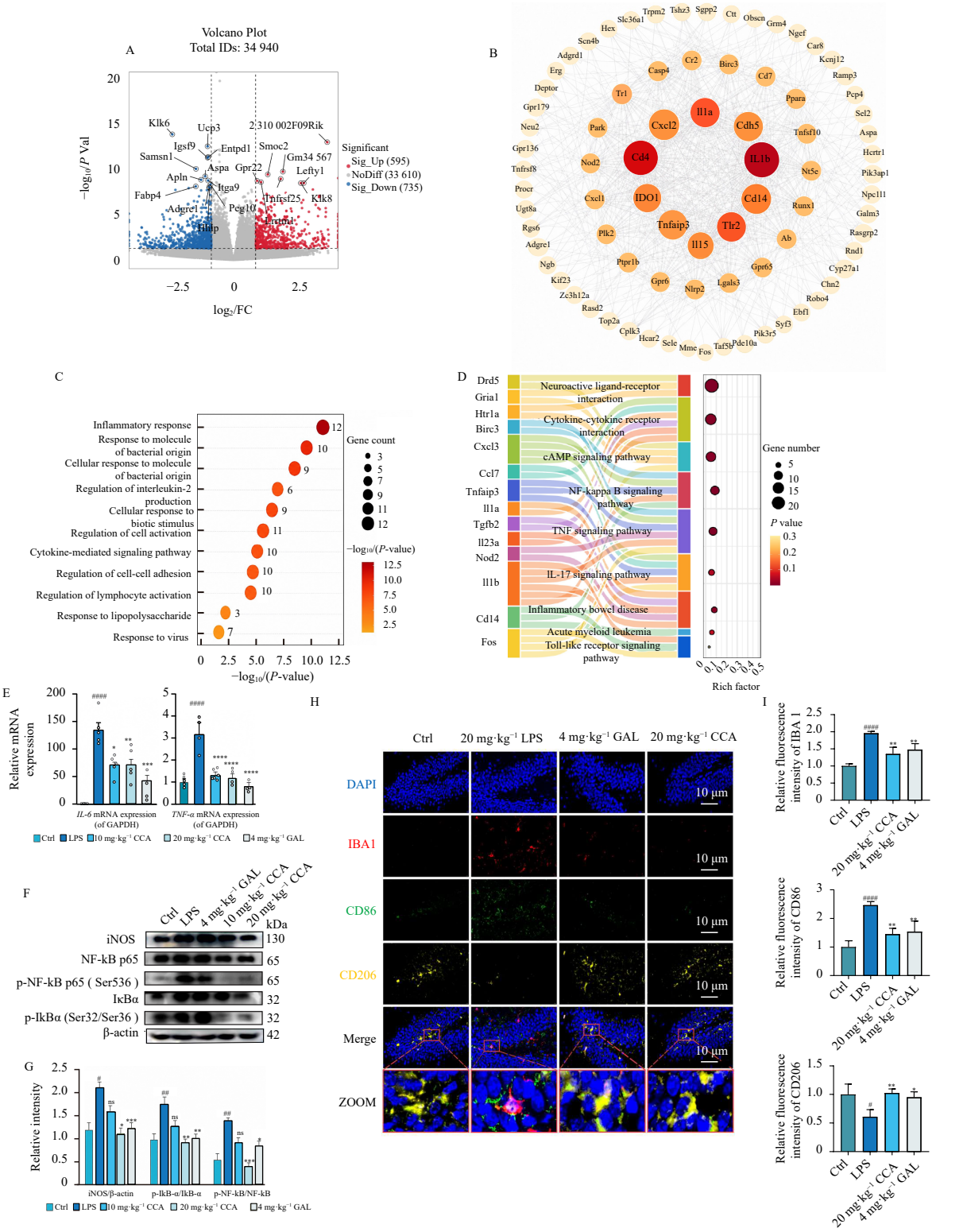


Fig. 3 CCA alleviates the neuroinflammation in LPS-induced mice. (A) The volcano plot RNA-seq. (B) PPI analysis of DEGs. (C) GO_BP enrichment analysis. (D) Sankey analysis of DEGs. (E) The mRNA levels of the pro-inflammatory factors IL-6 and TNF-α, $n = 5$. (F) Detection the expressions of iNOS and NF-κB pathway-related proteins by Western blotting, with quantification (G). (H) The presentative fluorescence photographs of IBA1, CD86, and CD206 in the dentate gyrus region, with quantification shown in (I), scale bars:10 μm. All the data are presented as the mean ± SD. One way ANOVA followed by Tukey's multiple comparisons test was conducted in the statistical analysis. $^{\#}P < 0.05$, $^{\#\#}P < 0.01$, $^{\#\#\#}P < 0.001$, $^{\#\#\#\#}P < 0.0001$ *vs* ctrl group. $^{*}P < 0.05$, $^{**}P < 0.01$, $^{***}P < 0.001$, $^{****}P < 0.0001$ *vs* LPS group, *ns* denotes no significant.

promote microglial polarization from M1 to M2 phenotype. Together, our findings suggested that CCA might exert its anti-inflammatory effects by modulating the NF-κB classical signaling pathway, as well as promoting microglial polarization toward the M2 type, which providing the anti-neuroinflammation effect in LPS-induced mice.

3.5. CCA alleviated cognitive deficits and intracerebral inflammation in APP/PS1 mice

Furthermore, we investigated the effect of CCA on 8-month-old APP/PS1 AD transgenic mice. Flowchart of experimental procedures as show in Fig. 4A. The MWM assay revealed that the es-

cape latency of APP/PS1 mice was significantly longer than that of WT mice, indicating impaired spatial learning and memory. However, CCA treatment significantly reduced the escape latency in APP/PS1 mice (Figs. 4B&4C). The qPCR analysis demonstrated that the mRNA expression of pro-inflammatory cytokines, including IL-1β, IL-6, and TNF-α, were markedly elevated in the hippocampus of APP/PS1 mice compared to WT mice. Notably, CCA administration significantly attenuated the mRNA expression of these inflammatory factors (Fig. 4D). The IHC analysis showed that the mean optical densities of IL-1β (Figs. 4E&4F), IL-6, iNOS and TNF-α were increased in the cortex and hippocampus particularly in the CA1 and CA3 subregions of APP/PS1 mice compared with WT mice. In contrast, CCA treatment led to a significant reduction in the optical density of these cytokines in the same brain regions, suggesting a robust anti-inflammatory effect of CCA in AD mice (Fig. 4G). Finally, we assessed the regulatory effects of CCA on the protein expression of NF-κB signaling pathway in both the cortex and hippocampus. Western blot results indicated that CCA treatment significantly revealed the phosphorylated NF-κB and IκB, compared to the untreated APP/PS1

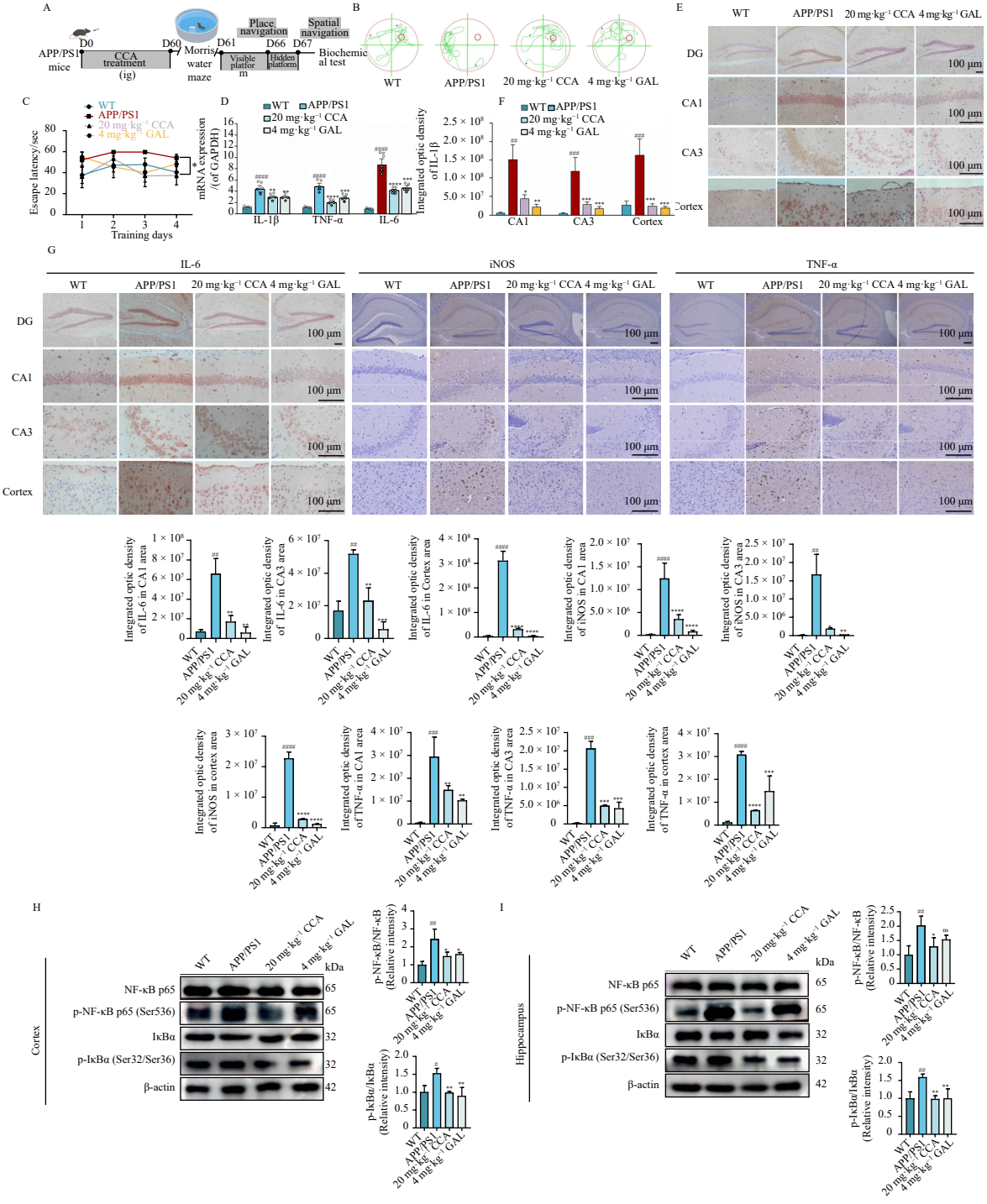


Fig. 4 CCA ameliorated cognitive deficits and neuroinflammation in APP/PS1 mice. (A) Flowchart of experimental procedures. (B) Representative images of trajectory. (C) The escape latency of each group mice. (D) The mRNA levels of pro-inflammatory factors IL-1β, IL-6, and TNF-α in the hippocampus of APP/PS1 mice. (E–F) IHC results of IL-1β and the quantification, scale bars:100 μm. (G) IHC results of IL-6, iNOS and TNF-α, scale bars:100 μm. Western blot of NF-κB pathway-related proteins in cortex (H) and hippocampus (I), $n = 3$. The error bars denote the standard deviation. All the data are presented as the mean ± SD. One way ANOVA followed by Tukey's multiple comparisons test was conducted in the statistical analysis. $^{\#}P < 0.05$, $^{\#\#}P < 0.01$, $^{\#\#\#}P < 0.001$, $^{\#\#\#\#}P < 0.0001$ *vs* WT group. $^{*}P < 0.05$, $^{**}P < 0.01$, $^{***}P < 0.001$, $^{****}P < 0.0001$ *vs* APP/PS1 group, *ns* denotes no significant.

group (Figs. 4H&4I). Taken together, these findings suggested that CCA ameliorated cognitive deficits and suppressed neuroinflammation in APP/PS1 mice, potentially through modulation of the NF-κB signaling pathway.

3.6. CCA facilitated the polarization of microglia from M1 to M2 phenotype in APP/PS1 mice

Excessive microglial activation can lead to the release of pro-inflammatory mediators such as TNF-α, IL-1β, IL-6 and NO, activate the NF-κB pathway, trigger activation of the NF-κB signaling pathway, create a chronic inflammatory environment, and ultimately result in neuronal damage, synaptic loss, and sustained neuroinflammation [26, 27]. Figs. 5A&5B showed that, compared to the APP/PS1 group, the fluorescence intensity of the microglial marker IBA1 and the astrocytic marker GFAP in the DG region of the hippocampus was significantly reduced in APP/PS1 mice treated with CCA. Furthermore, we conducted Sholl analysis to characterize the shape of IBA1 expressing cells. The branching of microglia in APP/PS1 mice was significantly reduced, indicating that it was activated. The branching of microglia increased significantly after CCA treatment, which indicated that the activation of microglia was inhibited. (Fig. 5C). IHC analyses revealed that the expression level of IL-10 (the marker of M2-type polarization of microglia) in the cortex and hippocampus of CCA-treated APP/PS1 mice particularly in the CA1 and CA3 regions were markedly increased (Figs. 5D&5E). Moreover, the levels of phosphorylated tau (Thr181) in the cortex and hippocampus of CCA-treated APP/PS1 mice were significantly decreased (Figs. 5D&5E). Additionally, IHC indicated that the M2-type microglia marker CD206 was significantly upregulated in CCA group (Figs. 5F&5G), whereas the expression of the M1 phenotypic marker CD86 was substantially downregulated in CCA group (Figs. 5F&5G). These findings collectively indicate that CCA could inhibit the excessive activation of microglia and astrocytes, promote the polarization of microglia from the M1 to the M2 phenotype, and thereby reduced abnormal tau phosphorylation in APP/PS1 mice.

3.7. CCA could up-regulate the expression of FOXG1 in APP/PS1 AD mice

To further investigate the mechanisms by which CCA allevi-

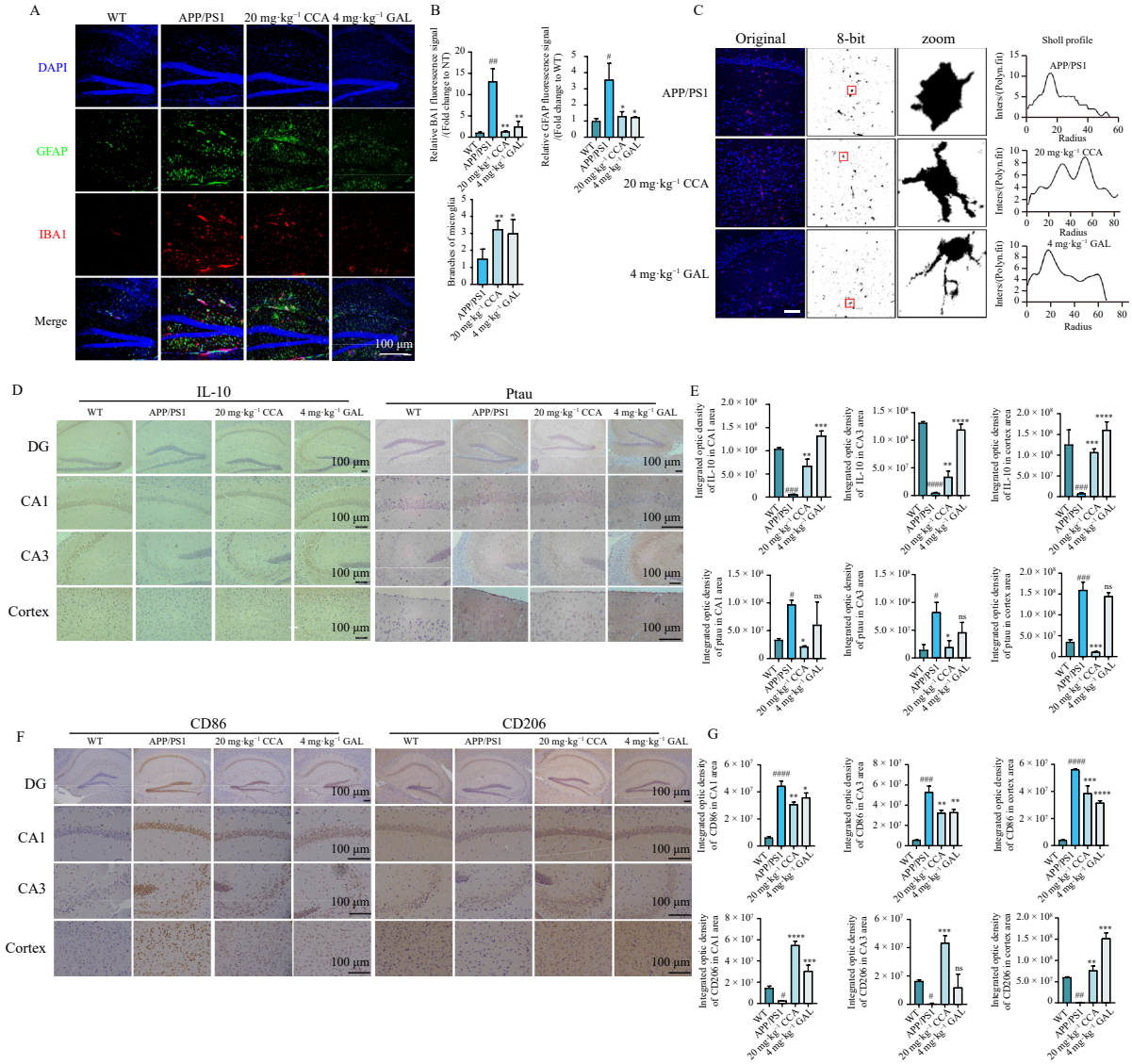


Fig. 5 CCA promotes the polarization of microglia from M1 to M2. (A) The IF of IBA1 and GFAP fluorescence intensifications in the dentate gyrus region of the brain in APP/PS1 mice, scale bars: 100 μm. The quantification of IF in (B). (C) Sholl Analysis of IBA1 positive cells in APP/PS1 mice or CCA treated APP/PS1 mice; scale bars: 50 μm. (D) IHC analysis of IL-10 and p-tau expression in hippocampus and cortex of APP/PS1 mice, with quantification shown in (E), scale bars: 100 μm. (F) IHC analysis of CD86 and CD206 expression in hippocampus and cortex of APP/PS1 mice, with quantification shown in (G), scale bars: 100 μm. All the data are presented as the mean ± SD. One way ANOVA followed by Tukey's multiple comparisons test was conducted in the statistical analysis.$^{\#}P < 0.05$, $^{\#\#}P < 0.01$, $^{\#\#\#}P < 0.001$, and $^{\#\#\#\#}P < 0.0001$ *vs* WT group. $^{*}P < 0.05$, $^{**}P < 0.01$, $^{***}P < 0.001$, $^{****}P < 0.0001$ *vs* APP/PS1 group, *ns* denotes no significant.

ates neuroinflammation in AD mice, we conducted a quantitative proteomics analysis using 4D-DIA technology. As shown in Fig. 6A, a total of 89 differentially expressed proteins (DEPs) were identified, including 20 up-regulated and 69 significantly down-regulated proteins. The heatmap demonstrated the expression patterns of these DEPs across multiple samples (Fig. S2A). KEGG pathway enrichment analysis revealed that the top pathways included the pentose phosphate pathway, cAMP signaling pathway, FOXO signaling pathway, Alzheimer's disease pathway, neurodegenerative disease pathways, and axon guidance, among others (Fig. S2D). GO analysis indicated that the top biological processes associated with DEPs included acute inflammatory response, inflammatory response, glial cell differentiation, and regulation of the immune system (Fig. 6B). In terms of CC, the enriched categories included cholinergic receptor activity, neurotransmitter receptor activity, NADH binding, and amino acid transmembrane transporter activity. MF were predominantly associated with acetylcholine-gated ion channels, myelin structure, and axonal components (Fig. S2B&2C). The top terms associated with the Sankey plot include myelin formation, regulation of glial cell differentiation, regulation of dopamine secretion, oxidative stress pathways, the redox pathway, and the acute-phase response. The principal proteins identified are Mag, Shank3, Dtnbp1, and Foxg1 (Fig. 6C).

We performed correlation analysis of differentially expressed proteins and their associated differentially expressed transcripts between two or more groups of samples, comparing the same or different expression trends of proteins and their associated transcripts. In the CCA_*vs*_MODEL group, for all quantitative proteins and their associated transcripts, we performed as-

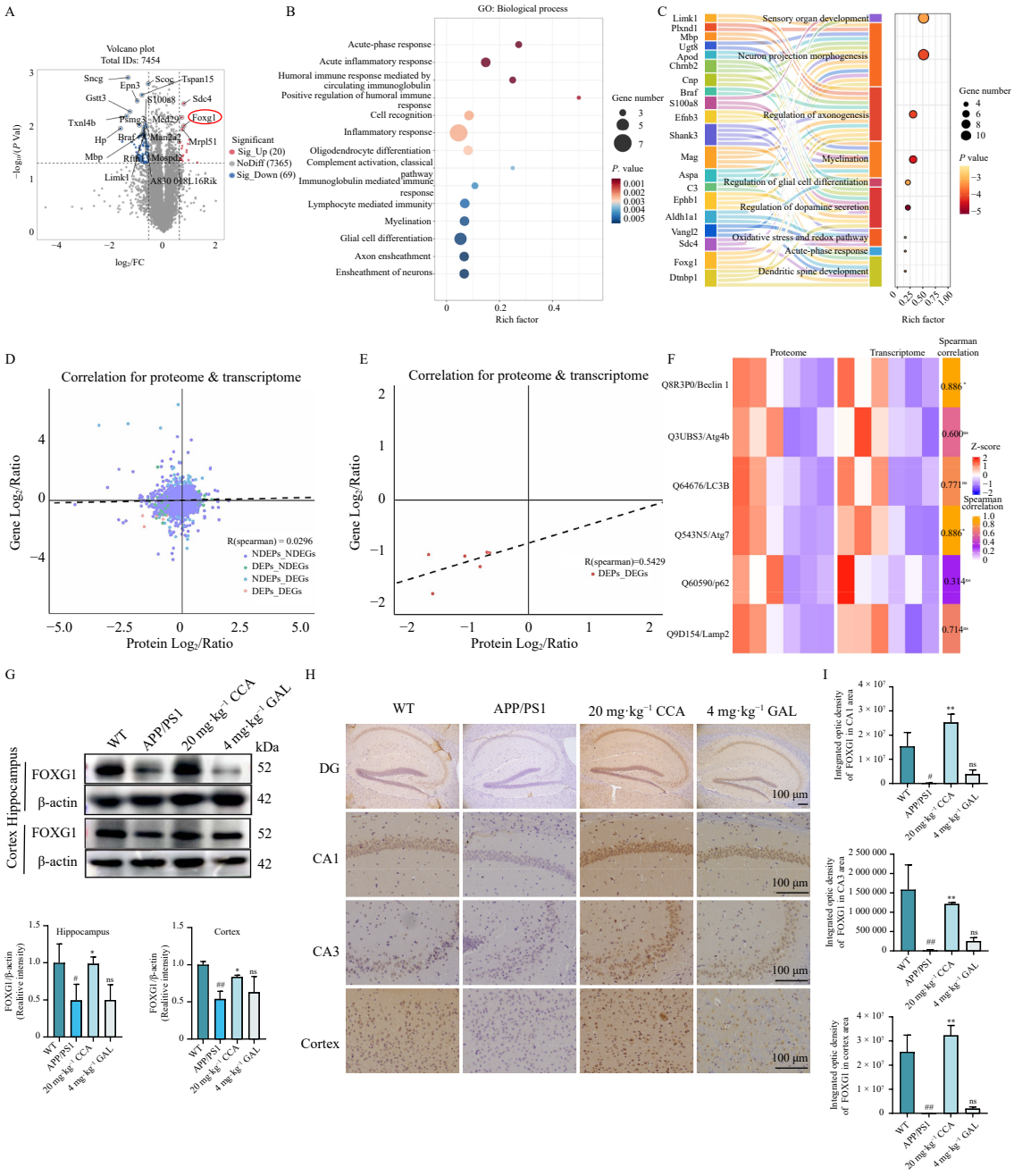


Fig. 6 Combined analysis and functional verification of proteomics and transcriptomics. (A) The volcanic plot of proteome. (B) Enriched terms of GO biological processes. (C) The Sankey plot of DEPs. (D) Scatter plot showing the correlation between expression levels of all quantified proteins and their associated genes. (E) Differentially expressed proteins (DEPs) and their associated differentially expressed genes (DEGs). (F) Analysis of the association between differential transcription and specific protein expression. (G) The expression of FOXG1 proteins in the hippocampus and cortex of mice by Western blot and quantification. (H) IHC analysis of FOXG1 in hippocampus and cortex of APP/PS1 mice and the quantification (I), scale bars: 100 μm. All the data are presented as the mean ± SD. One way ANOVA followed by Tukey's multiple comparisons test was conducted in the statistical analysis. $^{\#}P < 0.05$ and $^{\#\#}P < 0.01$ *vs* WT group. $^{*}P < 0.05$ and $^{**}P < 0.01$ *vs* APP/PS1 group, *ns* denotes no significant.

sociation, with a correlation coefficient of 0.0296 (Fig. 6D). For significantly differentially expressed proteins and significantly differentially expressed genes, we performed association, with a correlation coefficient of 0.5429 (Fig. 6E). For significantly different proteins and significantly different genes, we performed association and calculated the correlation coefficient for each pair of different genes and different proteins. The results showed that Becn1, Atg4b, Map1lc3b, Atg7, Sqstm1, and Lamp2 had strong correlations in transcriptomics and proteomics, especially Becn1 and Atg7 (Fig. 6F). These are autophagy-related genes. Additionally, we also conducted GSEA analysis. The results showed that GOBP_POSITIVE_REGULATION_OF_TOR_SIGNALING was significantly upregulated (NES: 1.989, P: 0.00033, FDR: 0.05067)(Fig S3). This indicates that the AMPK/mTOR/autophagy axis has been activated. Based on the above results, CCA may activate autophagy through the AMPK–mTOR–ULK1 axis.

FOXG1 positively regulates cell survival and autophagy within the nervous system. It is also involved in dendritic spine development, axon formation regulation, and neuronal process maturation, among other functions [28, 29]. Western blot result showed that the expression of FOXG1 was significantly increased in CCA group both in cortex and hippocampus (Fig. 6G). IHC analysis also revealed a significant decrease in FOXG1 expression in the hippocampus of APP/PS1 mice compared to the WT group. However, FOXG1 expression was notably elevated in the hippocampus of CCA-treated APP/PS1 mice (Figs. 6H&6I). These suggested that the inhibition of neuroinflammation by CCA may be related to the up-regulation of FOXG1.

3.8. CCA activates autophagy in microglia via AMPK-mTOR signaling pathway in APP/PS1 AD mice

There exists a multi-level functional interplay between FOXG1 and AMPK, with their interactions demonstrating particular significance in the processes of neuroprotection and autophagy modulation [30]. We further examined the expression levels of proteins in the AMPK/mTOR signaling pathway in the hippocampus of APP/PS1 mice following CCA treatment. The results demonstrated that CCA significantly upregulated the expression of p-AMPK while downregulating the expression of p-mTOR in both the cortex and hippocampus in APP/PS1 mice (Figs. 7A&7B). The IHC results also indicated that after CCA treatment, the expression levels of p-AMPK in the CA3 region of the hippocampus of APP/PS1 mice significantly increased, as well as the cortex (Fig. S2E). It has been reported that FOXG1 activated the AMPK-mTOR autophagy pathway [30]. Next, we examined the effect of CCA on autophagy in APP/PS1 mice. Western blot results revealed a significant increase in the LC3-II/LC3-I ratio and a notable decrease in p62 levels following CCA treatment in APP/PS1 mice (Fig. 7C). Furthermore, the IHC analysis demonstrated that, in comparison to APP/PS1 mice, the expression levels of LC3 in the cortex and hippocampus were markedly elevated in mice treated with CCA (Figs. 7D&7E), whereas the expression level of p62 was significantly reduced (Fig. 7F&7G). These findings indicated that CCA was capable of activating the AMPK/mTOR signaling pathway, as well as enhancing autophagy.

3.9. CCA promotes autophagy through the activation of the AMPK/mTOR/FOXG1 pathway

We next further explored the mechanism of autophagy activation by CCA. As illustrated, CCA administration induced an autophagy activation response comparable to that of the autophagy activator rapamycin in LPS-induced BV2 cells. In comparison to the LPS group, CCA treatment resulted in a significantly increase in LC3 fluorescence intensity and markedly reduced p62 fluorescence intensity (Fig. 8A&8B). To further investigate the effect of CCA on autophagy, we used Transmission electron microscopy (TEM) to examine the autophagosomes and autolysosomes in BV2 cells. After administering CCA, compared with the LPS group, more autophagosomes and autolysosomes were observed in BV2 cells, suggesting the activation of autophagy in BV2 cells (Fig. 8C). Following the administration of chloroquine, an autophagy inhibitor, autophagic flux was enhanced, leading to elevated fluorescence intensities of both LC3B and p62, indicating that CCA-induced autophagy was effectively blocked. Western blot analysis revealed that the LC3II/I ratio and the expression level of FOXG1 were substantially increased after CCA treatment, whereas the level of p62 was decreased (Figs. 8D&8E). These findings suggest that CCA may exert neuroprotective effects in BV2 cells by promoting autophagy.

To further investigate whether CCA activates the AMPK/mTOR-mediated autophagy pathway, BV2 cells were co-treated with CCA and 10 μmol·L^{-1} BML-275 (an AMPK inhibitor) for 24 h. The expression levels of key proteins in the AMPK/mTOR signaling pathway were then analyzed by Western blot. The addition of BML-275, as opposed to CCA treatment alone, attenuated the activation of the AMPK/mTOR pathway and autophagy induced by CCA, and also reduced the expression of FOXG1 (Figs. 8F&8G). Furthermore, BML-275 was found to reverse the CCA-induced the down-regulation of the pro-inflammatory proteins IL-6, IL-1β, and TNF-α induced by CCA (Fig. 8H). Taken together, these data indicated that CCA might activate the autophagy through AMPK/mTOR/FOXG1 pathway and reduced inflammatory factor levels achieved through the AMPK/NF-κB pathway, thereby providing a protective effect against neuroinflammation.

We conducted molecular docking to identify the target of CCA. Our results indicated that CCA was unable to form a stable interaction with FOXG1; however, it demonstrated the capacity to form a stable interaction with AMPK. AMPK can mediate autophagy *via* signaling cascades and modulate inflammation through downstream signaling pathways [31, 32]. We hypothesize that AMPK may serve as a crucial target for CCA to enhance autophagy and provide anti-neuroinflammatory effects. Molecular docking results indicated that Asn48 formed hydrogen bonds with the acetoxy groups of CCA, LYS29 participates in cationic interactions, while PHE27, IlE46, ILE52, LEU47 and VAL24 contribute to the formation of hydrophobic pockets. The extensive hydrophobic effect provides the main binding free energy for the binding process. CCA can stably insert into the binding pocket of the target protein, collectively maintaining conformational stability (Fig. 9A). MD results indicated that, the interaction between the protein receptor and the ligand remained relatively stable over 100 ns with no significant deviations observed within the range of 0–3.6 Å (Fig. 9B). The RMSF values of amino acid residues in the ligand-binding pocket region (marked by the green vertical line) have significantly decreased, indicating that the interaction between CCA and the target protein AMPK effectively restricts the local conformational fluctuations of the binding interface, significantly enhancing the structural rigidity and conformational stability of the binding region. This suggests that the conformational stability of the ligand-binding region is good, without any abnormal and intense conformational fluctuations, and indirectly reflects the binding stability of the ligand-protein complex (Fig. S4A). This stacked bar graph quantifies the residue-specific occupancy of three classical non-covalent forces at the protein-ligand binding interface through molecular dynamics trajectories, revealing a hierarchical cooperative bridge network. These forces jointly form a multi-level collaborative regulatory network, effectively resisting the competitive dissociation of water molecules and the conformational fluctuations of the protein binding pocket. Ultimately, this ensures that in the molecular dynamics simulation process, CCA can stably embed in the catalytic active pocket of AMPK (Fig. S4B). To validate this hypothesis, Cellular thermal shift assay (CETSA) assays were performed to further assess the stability of CCA and AMPK. The results revealed that compared to samples co-incubated with DMSO, the expression of AMPK in CCA-treated samples exhibited greater thermal stability at increasing incubation temperatures from 37 °C to 62 °C. (Fig. 9C) which suggesting a direct interaction between CCA and AMPK. These findings indicated that AMPK might be a potential

therapeutic target for CCA in the treatment of Alzheimer's disease.

3.10. Simulated PRKAA1 knockout revealed its underlying mechanism

The UMAP visualization analysis based on the brain expression clustering modules derived from the Human Protein Atlas (HPA) revealed that PRKAA1(encode AMPK catalytic α1 subunit) exhibits a widespread and non-specific broad-spectrum expression pattern in the human brain, belonging to cluster 45 (non-specific). It is stably expressed in all major regions of the brain and various types of nerve cells, and is widely distributed (Fig. 9D). Single-cell RNA sequencing (scRNA-seq) can be used to determine the specific distribution of key targets within cells, while the scTenifoldKnk virtual knockout algorithm assesses the key roles of these genes in diseases. Therefore, the scTenifoldKnk was used to evaluate the impact of PRKAA1 on AD. The results showed that after the PRKAA1 gene was knocked out, a total of 500 genes were affected. Among them, the most severely affected genes included MTOR, NFKB1, RELA, NLRP3, TNF, IL1B and IL6. (Fig. 9E&F, Table.S4). GO enrichment analysis indicated that these genes were highly correlated with regulation of autophagy, immune system processes, autophagosome, and chemokine activity (Fig. 9G). KEGG analysis suggested significant differences in the NF-κB signaling pathway, AMPK signaling pathway, autophagy, Alzheimer's disease and pathways of neurodegeneration (mutiple diseases) (Fig. 9H). These results indicate that the PRKAA1 gene can regulate AD through inflammatory responses and autophagy, which is consistent with previous research findings.

4. Discussion

The present study elucidates the complex neuroprotective mechanisms through which the cassane diterpenoid CCA mitigates Alzheimer's disease (AD) pathology, with a particular emphasis on its regulatory effects on neuroinflammation and autophagy. Importantly, although structural analogs of CCA, including CA-E and M2, have exhibited significant therapeutic potential in models of ulcerative colitis by inhibiting the NF-κB and MAPK signaling pathways [12, 13], this study represents the first evidence demonstrating CCA's capacity to modulate microglial polarization within the context of AD.

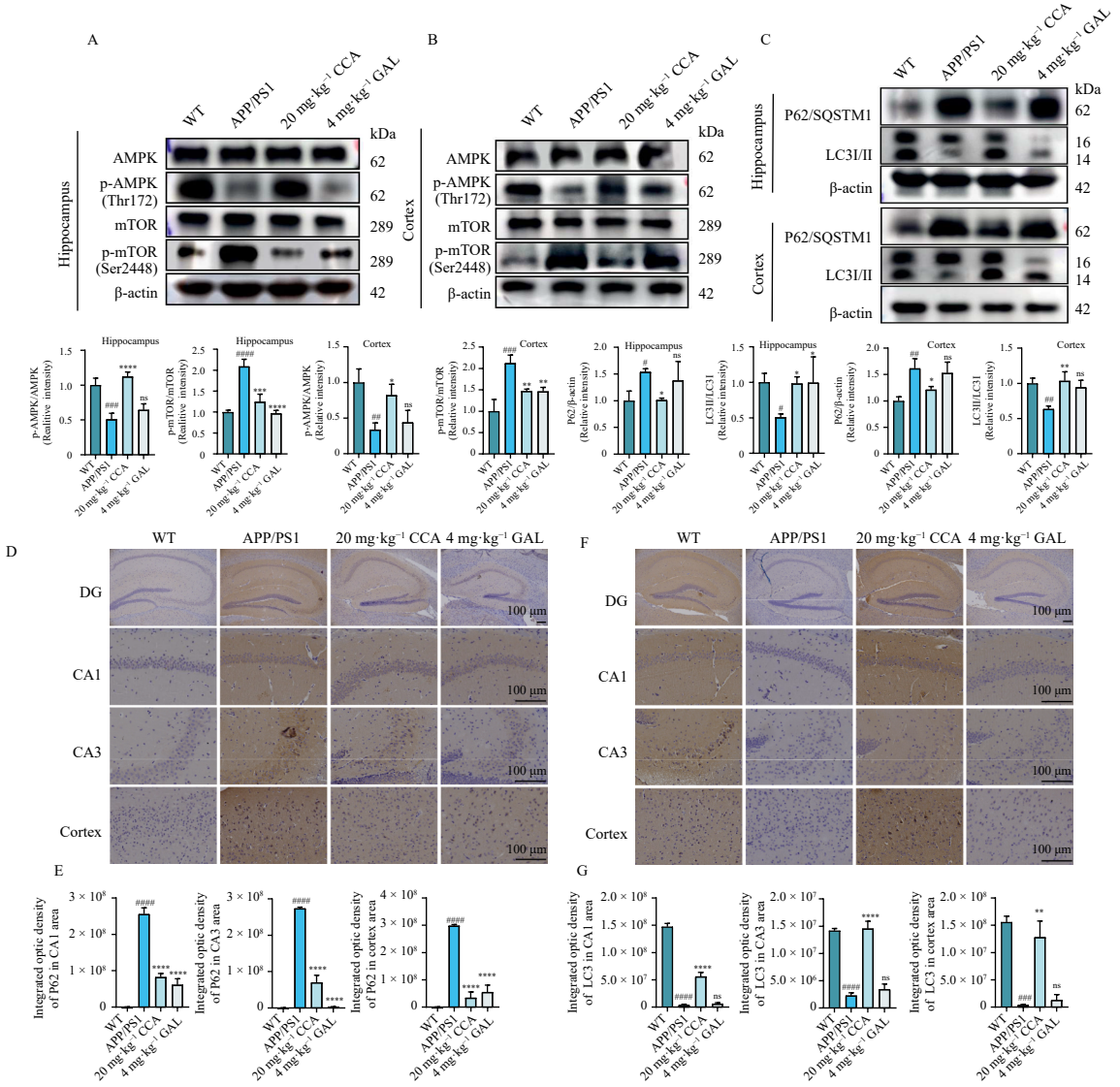


Fig. 7 CCA induced autophagy to mitigate neuroinflammation *via* AMPK/mTOR signaling pathway. The Western blot of AMPK/mTOR pathway-related proteins in the hippocampus (A) and cortex. (B). (C) The Western blot of LC3B and p62 proteins in the hippocampus and cortex. (D) The IHC of p62 proteins in the hippocampus and cortex and the quantification in (E), scale bars: 100 μm. (F) The IHC of LC3B proteins in the hippocampus and cortex and the quantification in (G), scale bars: 100 μm. All the data are presented as the mean ± SD. One way ANOVA followed by Tukey's multiple comparisons test was conducted in the statistical analysis. $^{\#}P < 0.05$, $^{\#\#}P < 0.01$, $^{\#\#\#}P < 0.001$, and $^{\#\#\#\#}P < 0.0001$ *vs* WT group. $^{*}p < 0.05$, $^{**}p < 0.01$, $^{***}P < 0.001$, $^{****}P < 0.0001$ *vs* APP/PS1 group, *ns* denotes no significant.

Neuroinflammation has emerged as a key focus in the study of neurodegenerative diseases in recent years. The activation of neuroinflammatory responses contributes to neuronal and synaptic damage as well as neuronal apoptosis, thereby accelerating the progression of AD [33]. As the primary immune effector cells within the central nervous system, microglia become overactivated in response to pathological stimuli and secrete pro-inflammatory cytokines, such as TNF-α and IL-6, which contribute to the acceleration of neuronal damage and cognitive decline [34]. This study demonstrates that the natural product CCA exhibits significant anti-inflammatory effects by inhibiting the activation of LPS-induced BV2 microglial cells. This mechanism mediated by activated AMPK to inhibit the NF-κB signaling pathway (Fig. 1& Fig. 8G)[35]. In both LPS-induced acute inflammation mouse models and APP/PS1 transgenic AD mouse models, CCA administration markedly improved spatial memory performance and reduced systemic inflammatory cytokine levels (Fig.2 & Fig. 4). Importantly, CCA not only suppresses the secretion of pro-inflammatory mediators but also facilitates the phenotypic transition of microglia from the M1 to M2 polarization state [36]. Furthermore,

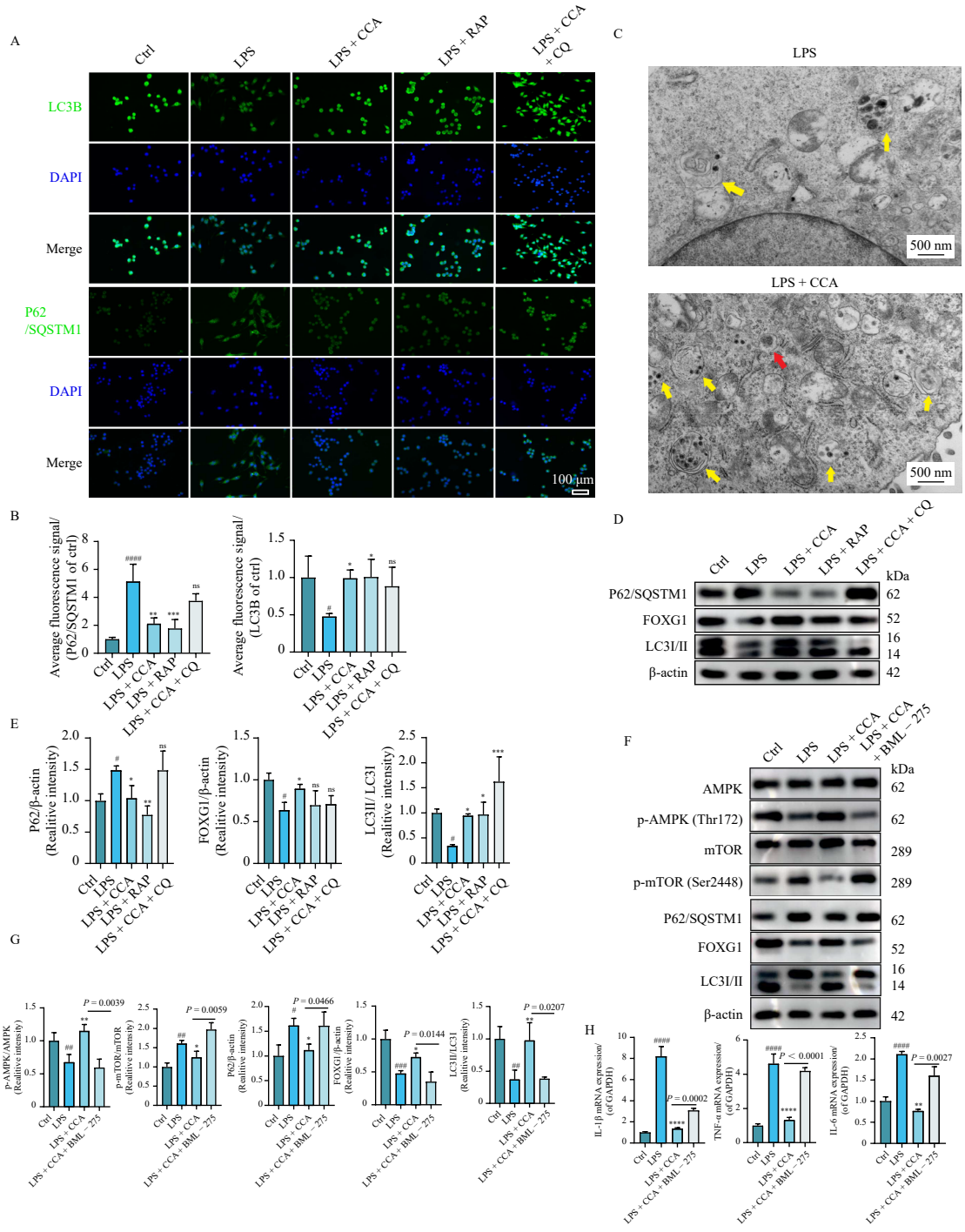


Fig. 8 CCA activate the autophagy in an AMPK-dependent manner. (A–B) The fluorescence levels of LC3B and p62 in BV2 cells and the quantification, scale bars: 100 μm.(C) Representative TEM images of BV2 cells, the yellow arrow indicates the autolysosomes, and the red arrow indicates the autophagosome, scale bars: 500 μm (D) Western blot of LC3I/II, FOXG1 and p62 in BV2 cells by following the administration of CCA (40 μmol·L^{-1}), the autophagy activator rapamycin (100 nmol·L^{-1}) and the autophagy inhibitor chloroquine (10 μmol·L^{-1}), with quantification in (E). (F) Western blot of AMPK/mTOR pathway-related proteins, as well as p62, LC3 Ⅰ / Ⅱ, FOXG1 in BV2 cells, followed by the addition of LPS and BML-275 for 24 h incubation, with quantification in (G). (H) The mRNA levels of pro-inflammatory transcription factors TNF-α, IL-6, and IL-1β were evaluated in BV2 cells. All the data are presented as the mean ± SD. One way ANOVA followed by Tukey's multiple comparisons test was conducted in the statistical analysis. $^{\#}P < 0.05$, $^{\#\#}P < 0.01$, $^{\#\#\#}P < 0.001$, $^{\#\#\#\#}P < 0.0001$ *vs* Ctrl group. $^{*}P < 0.05$, $^{**}P < 0.01$, $^{***}P < 0.001$, $^{****}P < 0.0001$ *vs* LPS group, *ns* denotes no significant.

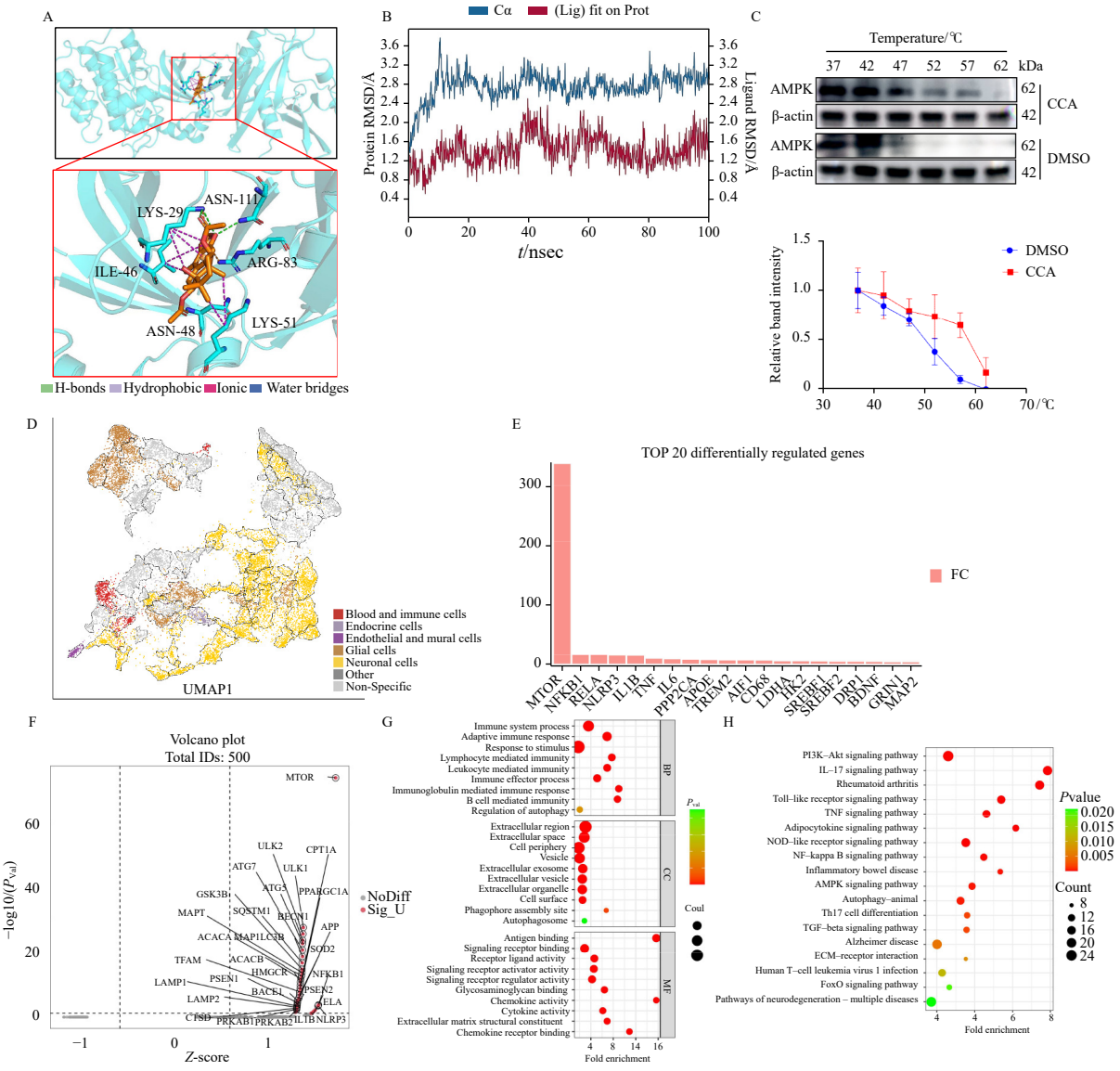


Fig. 9 The predicted and verified binding mode and interaction of CCA and AMPK. (A) The molecular docking between CCA and AMPK (PDB ID: 4CFE). (B) The MD of AMPK and CCA complex. (C) The CETSA experiment demonstrated the stability of the binding between CCA and AMPK. (D) UMAP visualization of PRKAA1 in the HPA brain expression clustering module. (E) Bar chart of genes significantly affected by PRKAA1 gene knockout. (F) Volcano plot of genes significantly affected by PRKAA1 gene knockout (p<0.05, |Z|>1.5). (G) GO enrichment analysis of genes significantly affected by PRKAA1 gene knockout simulation. (H) KEGG enrichment analysis of genes significantly affected by PRKAA1 gene knockout simulation.

PAMPA-BBB assay results indicate that CCA possesses excellent BBB permeability ($-Log_{Pe}$ = 5.4 cm·s^{-1}), a property closely associated with its molecular architecture featuring hydrophobic moieties and an optimal molecular weight (Table.1, Fig. 1A). This favorable BBB penetration capability provides a critical foundation for its therapeutic activity within the central nervous system.

Autophagy is a critical cellular process responsible for the degradation of dysfunctional organelles and misfolded or aggregated proteins. Accumulating evidence indicates that impairment of autophagy is closely linked to the pathogenesis of AD [37]. This study, for the first time, identified through quantitative proteomics that the expression of the transcription factor FOXG1 was significantly upregulated in the hippocampal tissue of APP/PS1 mice, which were verified by Western blot and IHC (Fig. 6). The FOXG1 gene is a member of the Forkhead box (FOX) family of transcription factors and plays a pivotal role in the regulation of cell proliferation and differentiation [38]. Previous investigations have demonstrated that FoxG1 exerts inhibitory effects on NLRP3-mediated neuroinflammation in both cellular and animal models of AD, while simultaneously modulating the AMPK/mTOR signaling pathway in a regulatory manner and promoting autophagic activity (Figs. 7A–7C) [30, 39]. Our study suggested that CCA treatment enhanced autophagic flux, evidenced by increased LC3-II/I ratio and decreased p62 levels in *vitro* and in *vivo*. Crucially, this effect was mediated through AMPK activation, as demonstrated by its reversal using the AMPK inhibitor BML-275 (Figs. 8D–8H). Molecular docking, CETSA, and molecular dynamics simulations further confirmed stable binding between CCA and AMPK, positioning AMPK as a primary target. Our data suggest that CCA promotes autophagy by activating AMPK, subsequently inhibiting mTOR and upregulating FOXG1 (Figs. 9A–9C). This cascade facilitates the clearance of phosphorylated tau and inflammasome activation, offering a dual therapeutic strategy against AD pathogenesis. Single-cell RNA sequencing (scRNA-seq) can provide a comprehensive cellular map, clearly determining the expression locations and distribution characteristics of core hub genes in specific cell types, thereby revealing the cell populations in which the target genes mainly exert their functions under physiological conditions. Based on this, the scTenifoldKnk virtual knockout algorithm can systematically simulate the inactivation of the target gene at the single-cell gene regulatory network level and quantitatively evaluate the global transcriptional changes, regulatory cascade reactions, and functional pathway changes caused by the absence of the target gene. Based on the HPA brain expression

clustering UMAP analysis, it was found that PRKAA1 is widely expressed throughout the brain in a broad spectrum and persistent form. The PRKAA1 gene was subjected to virtual knockout to simulate the biological effects of the absence of the PRKAA1 gene in vivo. After knockout, the gene was enriched in pathways related to autophagy and inflammation, confirming the previous viewpoint (Fig. 9E). However, this regulatory sequence (AMPK → mTOR → FOXG1) contrasts with the model proposed by Yun et al. (2024), which implicated FOXG1 upstream of AMPK/mTOR in modulating NLRP3 inflammasome activity in Aβ25-35 induced N2a cell [30]. This discrepancy may arise from differences in experimental models.

Microglia are recognized as key contributors to the pathogenesis and progression of AD, with emerging evidence suggesting their protective role against AD-associated premature mortality [37]. Accumulating data indicate that microglial autophagy may contribute to the mitigation of tau pathology [40]. NF-κB activation may upregulate mTOR expression and suppress the initiation of autophagy, whereas the sustained release of TNF-α by microglia can impair lysosomal function [41]. Impairment of autophagosome clearance leads to the accumulation of damaged mitochondria, which subsequently release excessive reactive oxygen species (ROS), thereby activating the NLRP3 inflammasome [34].

However, this study has several limitations. Although the acute LPS-induced neuroinflammatory model in BV2 microglial cells is valuable for initial screening, it has inherent limitations for Alzheimer's disease research as it fails to model chronic disease progression and neuronal pathophysiology.

5. Conclusion

In summary, our prior research shown that cassane diterpenoids with the same parent nucleus structure as CCA had significant anti-inflammatory properties, so establishing a platform for our investigation (Figs. 10). This study indicated that CCA activates AMPK, thereby simultaneously inhibiting the NF-κB pathway and upregulating the mTOR-FOXG1 pathway. This mechanism results in reduced pro-inflammatory cytokine production, neuronal protection, enhanced autophagic flux, and increased clearance of p-tau. It is supposed that CCA mitigates neuroinflammation through the inhibition of the AMPK/NF-κB pathway. Concurrently, CCA promotes autophagy by activating the AMPK/mTOR/FOXG1 pathway. These actions collectively contribute to the manifestation of an anti-Alzheimer's disease effect. This study confirmed the neuroprotective properties of CCA in Alzheimer's disease and offered novel insights into the potential of diterpenoids to enhance treatment through anti-neuroinflammatory mechanisms and the promotion of autophagy.

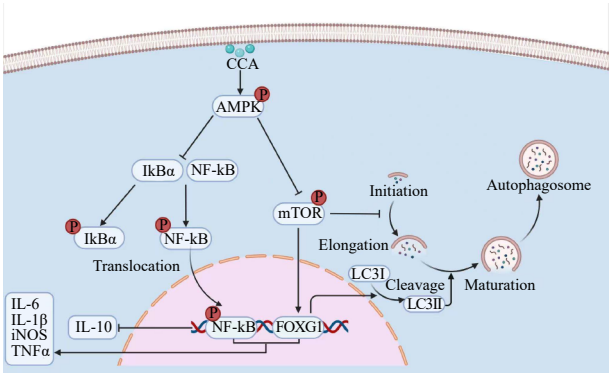


Fig. 10 The mechanism diagram of CCA in anti-neuroinflammation and activation of autophagy.

Fundings

This work was supported by National Natural Science Foundation Project of China (No. 82505106), the Application Fundamental Research Initiative of Liaoning Province (No. 2025080130-JH2/1013), the Science and Technology Innovation Team Project of the Department of Education of Liaoning Province (No. LJ222510163002), and Natural Science Foundation Program of Liaoning Province (Doctoral Research Initiation Project) (Nos. 2024-BS-045, 2024-BS-078, 2025-BS-0732, 2025-BS-0758), Basic research project of Liaoning Provincial Department of Education (No. JYTMS20231365).

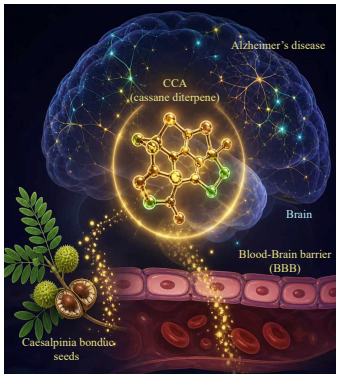
Declaration of Competing Interests

The authors have declared that no competing interest exist.

References

1 Scheltens P, De Strooper B, Kivipelto M, et al. Alzheimer's disease. *Lancet*. 2021;397(10284):1577-1590. https://doi.org/10.1016/S0140-6736(20)32205-4.
2 Bostancıklıoğlu M. An update on the interactions between Alzheimer's disease, autophagy and inflammation. *Gene*. 2019;705:157-166. https://doi.org/10.1016/j.gene.2019.04.040.
3 Gu YY, Liu MX, Zhao XR, et al. Cordycepin promotes autophagic degradation of α-synuclein *via* CacyBP/SIP activation for ameliorating olfactory dysfunction against Parkinson's disease. *Free Radic Biol Med*. 2025;238:522-541. https://doi.org/10.1016/j.freeradbiomed.2025.07.010.
4 Zhang XL, Gu YY, Liu YC, et al. Near-infrared enhanced organic Se-doped carbon nitride quantum dots nanozymes as SOD/CAT mimics for anti-Parkinson *via* ROS-NF-κB-NLRP3 inflammasome axis. *Chem Eng J*. 2024;499:156028. https://doi.org/10.1016/j.cej.2024.156028.
5 Zhang Z, Yang X, Song YQ, et al. Autophagy in Alzheimer's disease pathogenesis: therapeutic potential and future perspectives. *Ageing Res Rev*. 2021;72:101464. https://doi.org/10.1016/j.arr.2021.101464.
6 Terao I, Kodama W. Comparative efficacy, tolerability and acceptability of donanemab, lecanemab, aducanumab and lithium on cognitive function in mild cognitive impairment and Alzheimer's disease: a systematic review and network meta-analysis. *Ageing Res Rev*. 2024;94:102203. https://doi.org/10.1016/j.arr.2024.102203.
7 Colonna M, Butovsky O. Microglia function in the central nervous system during health and neurodegeneration. *Annu Rev Immunol*. 2017;35:441-468. https://doi.org/10.1146/annurev-immunol-051116-052358.
8 Hickman SE, Allison EK, El Khoury J. Microglial dysfunction and defective beta-amyloid clearance pathways in aging Alzheimer's disease mice. *J Neurosci*. 2008;28(33):8354-8360. https://doi.org/10.1523/JNEUROSCI.0616-08.2008.
9 Feng W, Zhang Y, Wang Z, et al. Microglia prevent beta-amyloid plaque formation in the early stage of an Alzheimer's disease mouse model with suppression of glymphatic clearance. *Alzheimers Res Ther*. 2020;12(1):125. https://doi.org/10.1186/s13195-020-00688-1.
10 Michelucci A, Heurtaux T, Grandbarbe L, et al. Characterization of the microglial phenotype under specific pro-inflammatory and anti-inflammatory conditions: effects of oligomeric and fibrillar amyloid-beta. *J Neuroimmunol*. 2009;210(1-2):3-12. https://doi.org/10.1016/j.jneuroim.2009.02.003.
11 Li Z, Zhang Z, Yu B. Unlocking the therapeutic potential of natural products for Alzheimer's disease. *J Med Chem*. 2025;68(3):2377-2402. https://doi.org/10.1021/acs.jmedchem.4c03049.
12 Wang Y, Gao J, Yu Y, et al. A plant-derived glucocorticoid receptor modulator with potency to attenuate the side effects of glucocorticoid therapy. *Br J Pharmacol*. 2023;180(2):194-213. https://doi.org/10.1111/bph.15957.
13 Liu T, Li X, Ning Z, et al. Two new cassane-type diterpenoids from the seed kernels of *Caesalpinia bonduc* (Linn.) Roxb. and their anti-inflammatory activity. *Nat Prod Res*. 2022;36(15):3901-3908. https://doi.org/10.1080/14786419.2021.1896511.
14 Wang M, Yu S, Qi S, et al. Anti-inflammatory cassane-type diterpenoids from the seed kernels of *Caesalpinia sinensis*. *J Nat Prod*. 2021;84(8):2175-2188. https://doi.org/10.1021/acs.jnatprod.1c00233.
15 Liu T, Wang M, Qi S, et al. New cassane-type diterpenoids from kernels of *Caesalpinia bonduc* (Linn.) Roxb. and their inhibitory activities on phosphodiesterase (PDE) and nuclear factor-kappa B (NF-κB) expression. *Bioorg Chem*. 2020;96:103573. https://doi.org/10.1016/j.bioorg.2020.103573.
16 Liu W, Liu X, Tian L, et al. Design, synthesis and biological evaluation of harmine derivatives as potent GSK-3β/DYRK1A dual inhibitors for the treatment of Alzheimer's disease. *Eur J Med Chem*. 2021;222:113554. https://doi.org/10.1016/j.ejmech.2021.113554.
17 Jiang X, Lu H, Li J, et al. A natural BACE1 and GSK3β dual inhibitor Notopterol effectively ameliorates the cognitive deficits in APP/PS1 Alzheimer's mice by attenuating amyloid-β and tau pathology. *Clin Transl Med*. 2020;10(3):e50. https://doi.org/10.1002/ctm2.50.
18 Wang X, Zhang J, Wang S, et al. Berberine modulates gut microbiota to attenuate cerebral ferroptosis induced by ischemia-reperfusion in mice. *Eur J Pharmacol*. 2023;953:175782. https://doi.org/10.1016/j.ejphar.2023.175782.
19 Wiśniewski JR, Zougman A, Nagaraj N, et al. Universal sample preparation method for proteome analysis. *Nat Methods*. 2009;6(5):359-362. https://doi.org/10.1038/nmeth.1326.
20 Liao X, Xie Q, Liang M, et al. Glucosidase alpha neutral C promotes influenza

virus replication by inhibiting proteosome-dependent degradation of hemagglutinin. *Signal Transduct Target Ther*. 2025;10:131. https://doi.org/10.1038/s41392-025-02227-6.
21 Li X, Li Y, Xiao J, et al. Unique DUOX2^{+} ACE2^{+} small cholangiocytes are pathogenic targets for primary biliary cholangitis. *Nat Commun*. 2023;14(1):29. https://doi.org/10.1038/s41467-022-34606-w.
22 Sherman BT, Hao M, Qiu J, et al. DAVID: a web server for functional enrichment analysis and functional annotation of gene lists (2021 update). *Nucleic Acids Res*. 2022;50(W1):W216-W221. https://doi.org/10.1093/nar/gkac194.
23 Huang DW, Sherman BT, Lempicki RA. Systematic and integrative analysis of large gene lists using DAVID bioinformatics resources. *Nat Protoc*. 2009;4(1):44-57. https://doi.org/10.1038/nprot.2008.211.
24 Mauersberger C, Schunkert H, Sager HB. Inflammation-related risk loci in genome-wide association studies of coronary artery disease. *Cells*. 2021;10(2):440. https://doi.org/10.3390/cells10020440.
25 Chen W, Yao S, Wan J, et al. BBB-crossing adeno-associated virus vector: an excellent gene delivery tool for CNS disease treatment. *J Control Release*. 2021;333:129-138. https://doi.org/10.1016/j.jconrel.2021.03.029.
26 Hansen DV, Hanson JE, Sheng M. Microglia in Alzheimer's disease. *J Cell Biol*. 2018;217(2):459-472. https://doi.org/10.1083/jcb.201709069.
27 Wang D, Zhang X, Wang M, et al. Early activation of astrocytes does not affect amyloid plaque load in an animal model of Alzheimer's disease. *Neurosci Bull*. 2018;34(6):912-920. https://doi.org/10.1007/s12264-018-0262-2.
28 Wang Z, Gu Y, Wang H, et al. FOXG1 interaction with SATB2 promotes autophagy to alleviate neuroinflammation and mechanical abnormal pain in rats with lumbar disc herniation. *Ann Med*. 2024;56(1):2399967. https://doi.org/10.1080/07853890.2024.2399967.
29 Wang Y, Tian M, Tan J, et al. Irisin ameliorates neuroinflammation and neuronal apoptosis through integrin αVβ5/AMPK signaling pathway after intracerebral hemorrhage in mice. *J Neuroinflammation*. 2022;19(1):82. https://doi.org/10.1186/s12974-022-02438-6.
30 Yun Q, Ma SF, Zhang WN, et al. FoxG1 as a potential therapeutic target for Alzheimer's disease: modulating NLRP3 inflammasome *via* AMPK/mTOR autophagy pathway. *Cell Mol Neurobiol*. 2024;44(1):35. https://doi.org/10.1007/s10571-024-01467-4.
31 Hardie DG, Ross FA, Hawley SA. AMPK: a nutrient and energy sensor that maintains energy homeostasis. *Nat Rev Mol Cell Biol*. 2012;13(4):251-262. https://doi.org/10.1038/nrm3311.
32 Steinberg GR, Hardie DG. New insights into activation and function of the AMPK. *Nat Rev Mol Cell Biol*. 2023;24(4):255-272. https://doi.org/10.1038/s41580-022-00547-x.
33 Singh D. Astrocytic and microglial cells as the modulators of neuroinflammation in Alzheimer's disease. *J Neuroinflammation*. 2022;19(1):206. https://doi.org/10.1186/s12974-022-02565-0.
34 Shi FD, Yong VW. Neuroinflammation across neurological diseases. *Science*. 2025;388(6753):eadx0043. https://doi.org/10.1126/science.adx0043.
35 Lu CS, Wu CY, Wang YH, et al. The protective effects of icariin against testicular dysfunction in type 1 diabetic mice *via* AMPK-mediated Nrf2 activation and NF-κB p65 inhibition. *Phytomedicine*. 2023;123:155217. https://doi.org/10.1016/j.phymed.2023.155217.
36 Wu H, Zheng J, Xu S, et al. Mer regulates microglial/macrophage M1/M2 polarization and alleviates neuroinflammation following traumatic brain injury. *J Neuroinflammation*. 2021;18(1):2. https://doi.org/10.1186/s12974-020-02041-7.
37 Litwiniuk A, Juszczak GR, Stankiewicz AM, et al. The role of glial autophagy in Alzheimer's disease. *Mol Psychiatry*. 2023;28(11):4528-4539. https://doi.org/10.1038/s41380-023-02242-5.
38 Hettige NC, Peng H, Wu H, et al. FOXG1 dose tunes cell proliferation dynamics in human forebrain progenitor cells. *Stem Cell Rep*. 2022;17(3):475-488. https://doi.org/10.1016/j.stemcr.2022.01.010.
39 Schmelzle T, Hall MN. TOR, a central controller of cell growth. *Cell*. 2000;103(2):253-262. https://doi.org/10.1016/S0092-8674(00)00117-3.
40 Xu Y, Propson NE, Du S, et al. Autophagy deficiency modulates microglial lipid homeostasis and aggravates tau pathology and spreading. *Proc Natl Acad Sci U S A*. 2021;118(27):e2023418118. https://doi.org/10.1073/pnas.2023418118.
41 Heneka MT, van der Flier WM, Jessen F, et al. Neuroinflammation in Alzheimer disease. *Nat Rev Immunol*. 2025;25(5):321-352. https://doi.org/10.1038/s41577-024-01104-7.



This cover artwork highlights CCA, a cassane diterpene derived from *Caesalpinia bonduc*, as a promising natural-product-based therapeutic candidate for Alzheimer's disease. The composition centers on a reserved space for a three-dimensional CCA molecular structure, envisioned in luminous gold, amber, and emerald-green tones, surrounded by a soft golden energy ring that emphasizes its central biological role. The pale gradient background evokes the cerebral microenvironment of neurodegeneration, with a translucent three-dimensional brain silhouette emerging subtly. Faint cyan and golden light trails weave through neural networks, symbolizing the complexity and vulnerability of neuronal pathways in the Alzheimer's brain. At the lower portion, minimalist illustrations of *Caesalpinia bonduc* seeds, fruits, and branches establish the botanical origin of CCA. Golden particles rise from the seeds and converge toward the central molecular space, representing the extraction and enrichment of the bioactive diterpene from its natural source. An abstract blood–brain barrier, depicted as closely packed endothelial cells, is integrated into the composition. Golden CCA-associated particles traverse this barrier into neural tissue, suggesting the compound's favorable blood–brain barrier permeability and ability to access the cerebral microenvironment. By combining botanical illustration, molecular visualization, vascular biology, and neural imagery, the cover presents an elegant and cohesive scientific portrayal of CCA as a natural compound of interest for Alzheimer's disease research.